1
Intrinsic Optical Properties of Diamond

Richard P. Mildren

Diamond comprises the lowest mass element that can form a stable covalently bonded crystal lattice, and this lattice is highly symmetric and tightly bound. Its resulting extreme properties, along with the recent developments in its synthesis, have led to an explosion of interest in the material for a diverse range of optical technologies including sensors, sources, and light manipulators. The optical properties in many respects sit well apart from those of other materials, and therefore offer the tantalizing prospect of greatly enhanced capability. A detailed knowledge base of the interaction of electromagnetic radiation with the bulk and the surface of diamond is of fundamental importance in assisting optical design.

For any material, the dataset characterizing optical performance is large and diamond is no exception despite its inherent lattice simplicity. The properties of interest extend over a large range of optical frequencies, intensities and environmental parameters, and for many variants of the diamond form including defect and impurity levels, crystal size, and isotopic composition. Over and above the fascination held for this ancient material, its highly symmetric structure and pure natural isotopic content (98.9% ^{12}C) provides an outstanding example for underpinning solid-state theory. As a result, diamond has been extensively studied and its optical properties are better known than most other materials.

Many excellent reviews of optical properties have been reported previously (see e.g. Refs [1–3]). These concentrate mainly on linear optical properties, often focus on extrinsic phenomena, and are written from perspectives outside of the field of optics, such as electronics and solid-state physics. Consequently, there is a need to consolidate the data from the perspective of optical design. Furthermore, the nonlinear optical properties of diamond have not to date been comprehensively reviewed. The aim of this chapter is to do this, with emphasis placed on the intrinsic properties of single-crystal diamond (i.e., pure Type IIa diamond[1)]). The chapter

1) Type IIa represents the most pure form; other categories (Types Ia, Ib, and IIb) have substantial levels of nitrogen (Type Ia and Ib) and/or boron impurity (Type IIb). Note that the delineations between types are not well defined. Type IIa are rarely found as large homogeneous crystals in nature as nitrogen aids the formation process. It is thus for historical reasons that nitrogen-doped diamonds, which provide the major source of natural gemstones, are categorized as Type I.

Optical Engineering of Diamond, First Edition. Edited by Richard P. Mildren and James R. Rabeau.

also includes the dependence of optical properties on basic variables such as wavelength, temperature, and isotopic composition. Although the scope is limited to bulk intrinsic properties, the intention is to stimulate a further expansion of the knowledge base as the limits of measurement resolution and performance are extended, and as more detailed investigations emerge into areas such as surface optics, crystal variants, and nano-optical effects.

The chapter focuses on the optical properties spanning from ultraviolet (UV) to infrared (IR). It should be noted that, throughout the chapter, Système Internationale (SI) units have been used, apart from some exceptions to stay with conventions. The data provided refer to diamond with the naturally occurring isotopic ratio, unless specifically stated otherwise.

1.1 Transmission

Diamond has a wide bandgap and lacks first-order infrared absorption, which makes it one of the most broadly transmitting of all solids. As shown in Figure 1.1, the transmission spectrum for a diamond window is featureless for wavelengths longer than approximately 225 nm ($\alpha < 1\,\mathrm{cm}^{-1}$ for $\lambda > 235\,\mathrm{nm}$), apart from a moderate absorption in the range 2.6 to 6.2 μm and extending weakly outside each side. Indeed, there is no absorption in the long-wavelength limit, which is a characteristic of the Group IV elements (e.g., Si and Ge) that share the diamond

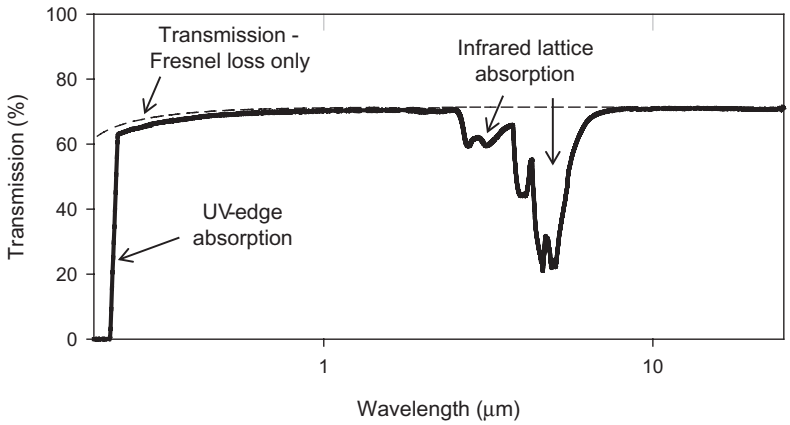

Figure 1.1 Transmission spectrum for a Type IIa diamond window ("Type IIIa," Element 6) of 1 mm thickness. The spectrum was measured using a Cary 5000 spectrometer (UV-near IR) and Bruker Zertex 80 (>2 μm; resolution 4 cm^{-1}). The transmission for Fresnel loss only (dashed curve) was calculated using the relation described in the text and in Equation (1.6). The small difference between the dashed and measured curves in the regions away from the UV-edge and lattice absorption is largely attributed to the combination of spectrometer calibration error and scatter in the sample.

lattice symmetry. UV-edge absorption, infrared lattice absorption and Fresnel reflection dominate the wavelength dependence for transmission. The Fresnel reflection at each diamond–air interface is approximately 17% in the visible ($R = 17.1\%$ at 632 nm), and when accounting for multiple reflections between each surface this leads to a maximum transmission of $(1 - R)^2/(1 - R^2) = 70.8\%$. Using dispersion data for the refractive index (see Section 1.4), the transmission upper limit (no absorption) is shown as a function of wavelength (dashed line in Figure 1.1).

1.2 Lattice Absorption

The absorption in the mid-IR, which is most prominent in the range 2.6 to 6.2 μm, arises due to the coupling of radiation with the movement of nuclei, and is often referred to as "lattice" or "multiphonon" absorption. The magnitude and shape of the absorption spectrum is a consequence of the vibrational properties of the crystal lattice, which are governed by the forces between neighboring atoms and the symmetry of collective vibrations. The theoretical framework that most successfully describes the spectrum has been developed since the 1940s, stimulated by the pioneering work of Sir C.V. Raman on diamond's optical properties and Max Born on the quantum theory of crystals. It is interesting to note that, although diamond's lattice is one of the most simple, there have been substantial controversies in explaining the spectrum (see e.g., Ref. [4]) and there are on-going challenges to thoroughly explain some of the features.

A brief and qualitative summary of the theory of lattice absorption is provided here to assist in an understanding of the IR spectrum's dependence on important material and environmental parameters such as impurity levels, isotopic content, and temperature. A greatly simplifying and important aspect is that there is no one-phonon absorption in pure, defect-free diamond (which would appear most strongly near 7.5 μm for diamond), as also for other monatomic crystals with inversion symmetry such as Si and Ge. The movement of nuclei in vibrational modes of the lattice are countered by equal and opposite movement of neighbors, so that no dipole moment for coupling with radiation is induced. One-phonon absorption may proceed by spoiling the local symmetry through, for example, lattice imperfections (impurities and defects) or by the application of electric field. Dipole moments may also be induced in the crystal via interaction of the incident photon with more than one phonon, although with reduced oscillator strength; this is the origin of lattice absorption in pure diamond. From a classical viewpoint, the absorption mechanism can be qualitatively understood as one phonon inducing a net charge on atoms, and a second phonon (or more) vibrating the induced charge to create a dipole moment [5]. The maximum phonon frequency that can be transmitted by the lattice is 1332 cm^{-1} (which corresponds to the zero-momentum optical phonon and the Raman frequency), and integer multiples of this frequency at 3.75 μm (2665 cm^{-1}) and 2.50 μm (3997 cm^{-1}) mark

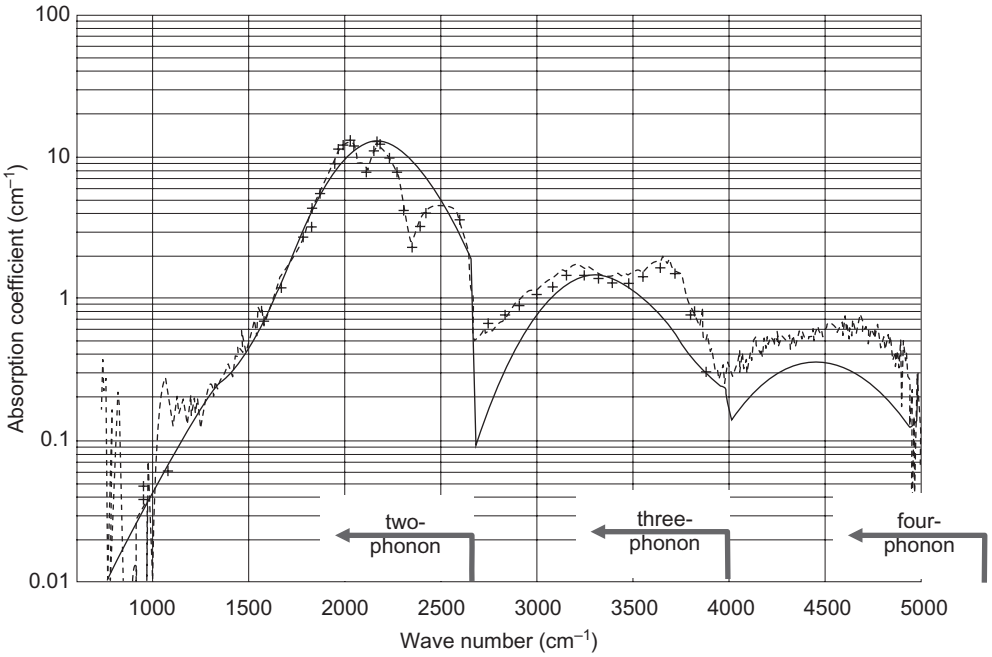

Figure 1.2 Two-, three-, and four-phonon lattice absorption bands. The underlying figure showing the calculated (smooth solid curve) and measured absorption spectra is reprinted with permission from Ref. [6]; © 1994, SPIE. The measurements were collated from several sources, as detailed in the reference.

the short-wavelength limits for two- and three-phonon absorption regions. The demarcations between two- and three-phonon absorption are clearly evident in the transmission spectrum of Figure 1.1 and the logarithmic plot of lattice absorption in Figure 1.2 [6]. Between wavelengths 3.75 and 6 μm, the lattice absorption at room temperature is strongest with a peak of approximately 10 cm^{-1} at 4.63 μm, and is primarily attributable to two-phonon absorption.

1.2.1 The Two-Phonon Region

Absorption may involve the creation and destruction of phonons, which are constrained to certain energies and wavevectors as a result of the symmetry and interatomic forces. For two-phonon creation, the absorption at a given frequency is proportional to the number of pairs of modes of the created phonons and a transition probability that takes into consideration allowed phonon combinations (e.g., longitudinal or transverse) and the transition oscillator strength. The number of allowed combinations of a given energy is usually highest for phonon wavevectors along directions of high symmetry in the lattice, and with momenta that

correspond to phonon wavelengths of the order of the atomic spacing in that direction (i.e., at the edge of the Brillouin zone). Along with the generally higher density of modes at the Brillouin zone edge, the transition probability is also higher as the largest charge deformations are induced. For diamond, there is also a peak in the density of modes in one symmetry direction (<110>) for momenta corresponding to wavevectors at approximately 70% of the Brillouin zone. These peaks in the density of states are the so-called "critical points" in the lattice phonon dispersion curves.

The primary directions of symmetry for the diamond lattice, along with the frequency of critical point phonons, are listed in Table 1.1. Also listed are the critical points derived from the relatively recent studies of Vogelsegang *et al.* [7] and Klein *et al.* [8], for data derived using a combination of neutron-scattering data, second-order Raman spectra[2)] [9] and, in the case of Ref. [8], by using impurity spectra to access single phonon information. There remains significant uncertainty in the frequency of many critical points, however, and as a result there is disagreement between some phonon assignments.

For temperatures below 1000 K, the populations of critical-point phonons are small (due to their characteristically high energies in diamond), and only phonon summations appear strongly in the spectrum. Momentum–energy conservation and symmetry impose selection rules for the type of phonons created. As the photon momentum is negligible compared to the Brillouin zone-edge phonons and to conserve crystal momentum, the wavevector of each phonon is equal in magnitude and opposite in direction. The character of the phonons must also be different; that is, they should correspond to different dispersion branches (either optical or acoustic phonon), or have a different polarization (longitudinal or transverse direction). The resulting absorption features are referred to as "combination lines." Pairs of phonons of the same type (overtones) are absent or weak.

Due to the large number of possible phonon modes, the spectrum appears as a fairly smooth continuum extending to wavelengths that extend beyond 10 μm. A joint-density-of-states calculation [10] was successful in reproducing the gross features of the two-phonon spectrum, as shown in Figure 1.3, including the broad peak near 2500 cm^{-1}, the region of highest absorption from 1800–2300 cm^{-1}, the local minimum at 2100 cm^{-1}, and the tail at frequencies less than 1750 cm^{-1}. An improved agreement would require a better knowledge of the dispersion curves and transition probabilities. Unfortunately, however, there are large uncertainties in the phonon dispersion data obtained by neutron scattering data, due to the lack of test samples of sufficient size. The more recently published critical point values [7, 8], obtained with the assistance of optical spectra of variable impurity and isotopic content, have enabled some features to be assigned to critical point

2) The second-order Raman scattering involves two phonons. The second-order spectrum contains a peak at twice the Raman frequency that is more than two orders of magnitude weaker than the first-order peak, and a broad feature extending to lower frequencies (see e.g., Ref. [9]).

Table 1.1 Directions of high symmetry, critical point phonons, the corresponding frequencies and two-phonon combinations identified in the IR absorption spectrum. Combinations corresponding to the major peaks are shown in bold. L = longitudinal, T = transverse, O = optical, and A = acoustic. Note that the use of L and T labels for the K symmetry points is not conventional and should not be taken as indicating branches of purely transverse or longitudinal character.

Crystal direction (as viewed in perspective through the 4 × 4 unit cell)	Crystal direction, K-space symmetry label	Critical point frequencies (cm^{-1})		Observed spectrum features in the two-phonon region (see Figure 1.4) with assigned phonon combinations (cm^{-1})
		Ref. [7]	Ref. [8]	
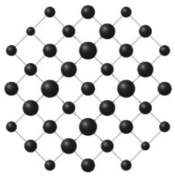	<100>, X	1170 (L)[a] 1088 (TO) 786 (TA)	1191 ± 3 (L)[a] 1072 ± 2 (TO) 829 ± 2 (TA)	2260 ± 6 L + TO (X) 1895 ± 6 TO + TA (X)[c]
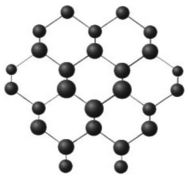	<110>, K	1236 (LO) 1112 (TO1) 1051 (TO2)[b] 986 (LA) 982 (TA1)[b] 748 (TA2)	1239 ± 2 (LO) 1111 ± 1 (TO1) 1042 ± 2 (TO2)[b] 992 ± 3 (LA) 978 ± 1 (TA1)[b] 764 ± 4 (TA2)	**1977 ± 2 LA + TA1 (Σ)** 2005.5 ± 2 LO + TA2 (Σ) **2029 ± 2 TO2 + (?)[d] (Σ)** 2097 ± 2 TO1 + LA (Σ) **2160 ± 2 TO1 + TO2 (Σ)** 2293 ± 8 LO + TO2 (Σ)
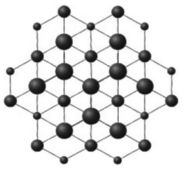	<111>, L	1245 (LO) 1208 (TO) 1009 (LA) 572 (TA)	1256 ± 4 (LO) 1220 ± 2 (TO) 1033 ± 2 (LA) 553 ± 2 (TA)	1777.5 ± 4 TO + TA (L) 1816.5 ± 4 TA + LO (L) 2260 ± 6 LA + (?)[e] (L) 2293 ± 6 LO + LA (L)
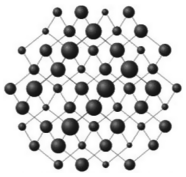	<210>, W	1164 (L)[a] 1012 (TO) 915 (TA)	1146 ± 1 (L)[a] 1019 ± 3 (TO) 918 ± 12 (TA)	2175 ± 5 L + TO (W)

a) The LO and LA modes are degenerate.
b) "Accidental" critical points occur for the TO2- and TA1-labeled phonons for wavevectors nearby the symmetry point.
c) Assignment agrees with Ref. [8] data only.
d) Ambiguous assignment – Ref. [8] suggests LA, whereas Ref. [7] suggests TA1.
e) Ambiguous assignment – Ref. [8] suggests LO, whereas Ref. [7] suggests TO.

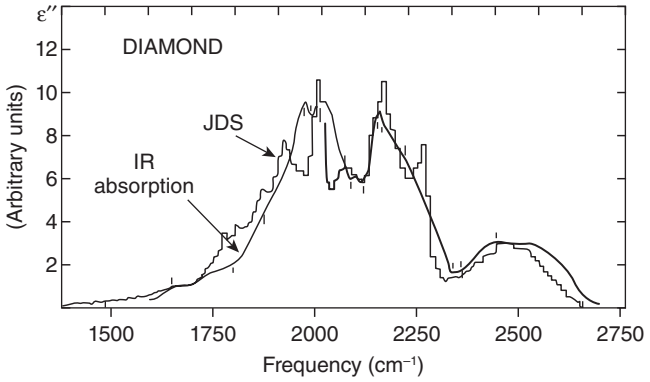

Figure 1.3 Comparison of two-phonon absorption band with the joint density of states (JDS) calculation of Wehner *et al*. [10], showing qualitative agreement with several of the main features in the measured spectrum. The stepped appearance of the calculated spectrum is a consequence of the digitizing procedure used to sample the phonon dispersion curves. Reproduced with permission from Ref. [10]; © 1967, Elsevier.

combinations with greater confidence. The last column in Table 1.1 lists the frequencies of features that can be readily seen in the spectrum of Figure 1.4, along with their suggested assignments of the likely critical point phonons. The major peaks at 4.63 μm (2160 cm^{-1}), 4.93 μm (2030 cm^{-1}) and 5.06 μm (1975 cm^{-1}) all correspond to phonons in the <110> symmetry direction, for which there is an "accidental" critical point in the dispersion curves for one or both of the phonons involved in the assigned combinations. A similar type of analysis can be performed, at least in principle, for the third- and higher-order phonon bands at wavelengths <3.75 μm (>2665 cm^{-1}); however, such a procedure is very difficult due to the greatly increased number of phonon combinations, the lack of detailed knowledge on transition probabilities, and the poor visibility of critical point locations.

1.2.2
Absorption at Wavelengths Longer than 5 μm

In the range 5 to 10 μm, lattice absorption decreases approximately exponentially from 10 cm^{-1} to approximately 0.05 cm^{-1}. The weaker longer-wavelength absorption results primarily from combination pairs of low-energy acoustic phonons away from the phonon dispersion critical points. A calculation for multiphonon absorption using polynomial fits to the acoustic phonon densities of states [6], reproduces this trend satisfactorily (as seen Figure 1.2). At wavelengths longer than 8 μm (<1250 cm^{-1}), a significant departure of experiment from theory is observed as the weaker absorption approaches the level of impurity absorption and the resolution of the measurement. Due to interest in diamond as a window

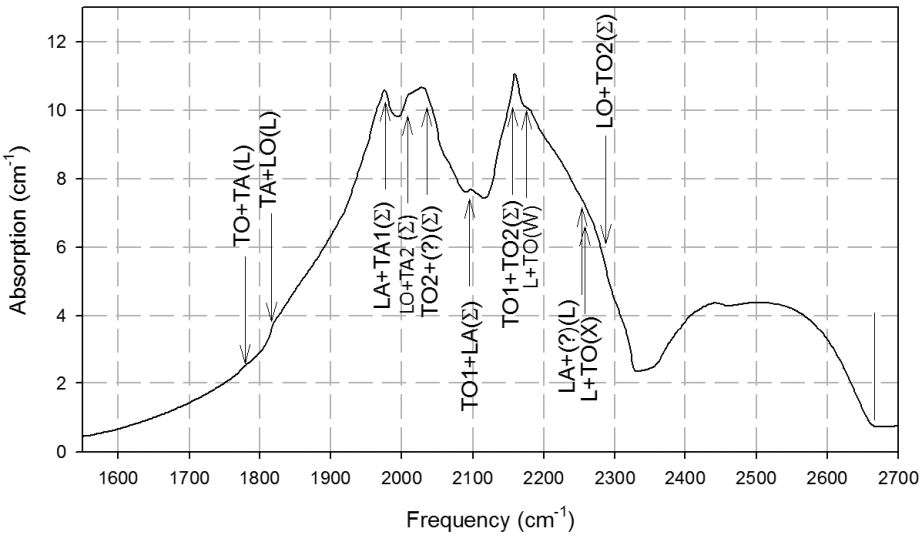

Figure 1.4 Detail of the two-phonon absorption region (using the data of Figure 1.1) with identification of major features in the spectrum with suggested critical point phonon summations (refer to Table 1.1). The vertical line at 2665 cm^{-1} corresponds to twice the Raman frequency, and indicates the upper limit for two-phonon absorption.

material for missile domes and high-power CO_2 lasers, absorption in the long-wavelength atmospheric window at 8–12 μm and at 10.6 μm has been studied in depth (see e.g., Refs [6, 11, 12]). Absorptions as low as 0.03 cm^{-1} at 10.6 μm have been measured for single-crystal and polycrystalline material [13]. Intrinsic absorption is expected to decrease monotonically at longer wavelengths *ad infinitum* due to the diminishing number of phonon modes and, indeed, low-loss material has been observed up to and beyond 500 μm [13, 14].

1.2.3
Temperature Dependence

Temperature affects lattice absorption via changes in the phonon ambient population density and shifts in phonon mode frequency. The effect of the thermal phonons in the material is to stimulate absorption events coinciding with the incident photon. As described by Lax [15], the relationship between two-phonon absorption coefficient α and temperature is given by

$$\alpha \propto (n_1 + 1)(n_2 + 1) \tag{1.1}$$

where n_i are the occupation numbers at thermal equilibrium of the final state phonons (also called Bose–Einstein factors)

$$n_i(\omega, T) = (\exp[\hbar\omega / k_B T] - 1)^{-1} \tag{1.2}$$

where k_B is Boltzmann's constant and $\hbar$ is Planck's constant divided by 2π. A further consideration noted by Lax was that of induced emission, which involves the annihilation of thermal phonons and the creation of an IR photon at the frequency sum. This is proportional to $n_1 n_2$ for two phonons, so that the net absorption becomes

$$\alpha \propto (n_1 + 1)(n_2 + 1) - n_1 n_2 = n_1 + n_2 + 1 \tag{1.3}$$

However, as $n_1 n_2$ can be neglected for temperatures less than approximately 1000 K, Equation (1.1) holds for most temperatures of interest. At room temperature and below, the density of thermal phonons is small so that absorption is essentially constant and reflects the spontaneous component (i.e., the component contribution caused by quantum fluctuations). At elevated temperatures, however, absorption increases notably (as shown in Figure 1.5a [16]) for temperatures up to 800 K and for wavelengths spanning the two- and three-phonon bands (from 2.5 μm to beyond 20 μm). The temperature dependence of a given feature in the absorption band varies slightly according to the thermal populations of the responsible phonons of the feature combination. Although the agreement with Equations (1.1) and (1.2) above is quite good for some spectral features [17], for others – such as those near the 4.9 μm peak – the increase in absorption exceeds the prediction. A more thorough treatment would need to consider contributions from higher-order multiphonon processes and also two-phonon difference bands (of frequency $\omega_i - \omega_j$, where the phonon ω_j is absorbed and ω_i phonon is emitted) which play an increasingly important role at higher temperatures and longer wavelengths [18].

Lattice absorption spectra between 2 and 20 μm for several temperatures up to 500 K are shown in Figure 1.5c. In addition to increased absorption by thermal phonons, the absorption spectrum is altered via small decreases in the phonon frequencies, which occur as a result of the change in interatomic forces and average atomic spacing. The shift varies according to the branches of the phonons involved, and is thus a complex function of wavelength. By using measurements of numerous absorption features, Picarillo *et al.* [18] determined that for the two-phonon region at temperatures between 14 and 825 K, the shifts of absorption features $\Delta\nu$ are within a maximum deviation of ±13% with the average fit given by

$$\Delta\nu/\nu = -0.027 \times n(\omega_e, T) \tag{1.4}$$

(where $\omega_e = 860\,\text{cm}^{-1}$) and which corresponds to approximately $0.013\,\text{cm}^{-1}\,\text{K}^{-1}$ at room temperature near 4 μm. The calculated temperature shift at the two-phonon peak ($2160\,\text{cm}^{-1}$) and experimental measurements for the nearby $2286.5\,\text{cm}^{-1}$ shoulder feature are shown in Figure 1.5b.

1.2.4 Isotopic Content

The effect of the isotopic ^{12}C to ^{13}C ratio on the spectrum on the two-phonon spectrum has been investigated [7]. As the ^{13}C content is increased from the

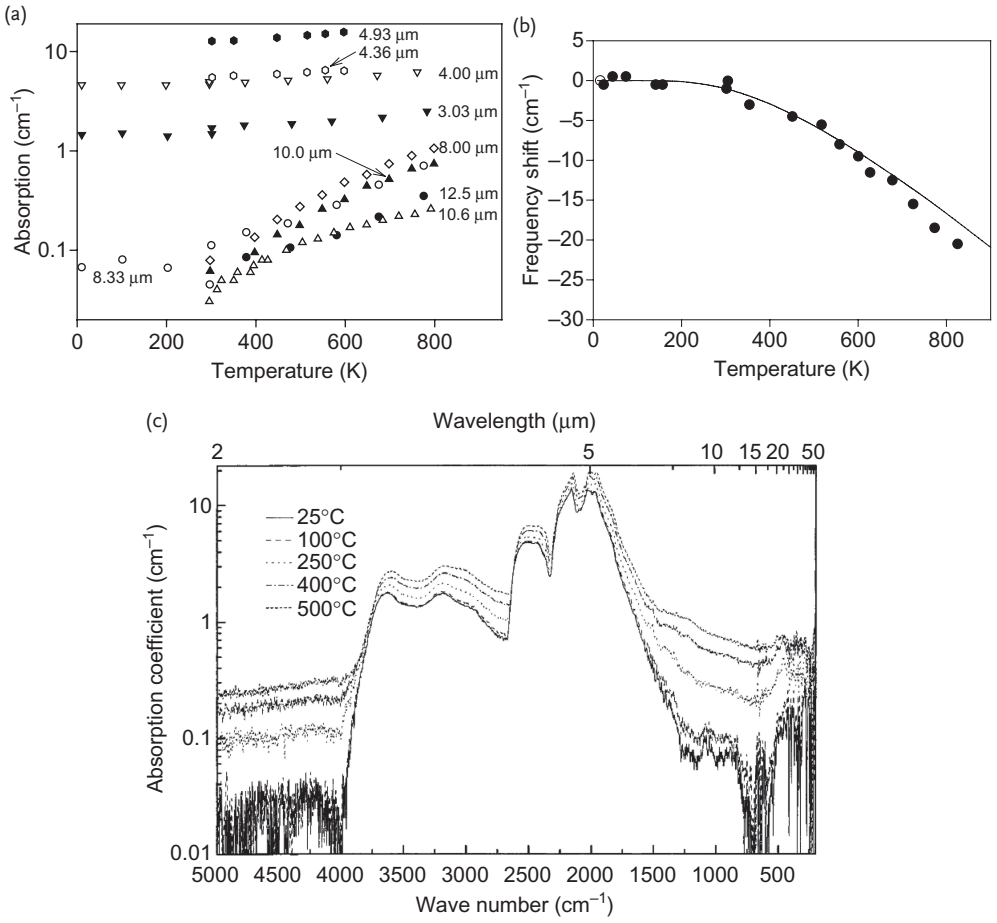

Figure 1.5 (a) Temperature dependence of absorption at selected IR wavelengths [11, 16–18]; (b) Shift of the 2286.5 cm^{-1} shoulder as a function of temperature in the two-phonon spectrum (data points [18]). The solid line is the calculated shift using Equation (1.4); (c) Lattice absorption spectrum as a function of temperature. Reproduced with permission from Ref. [11]; © 2003, Institute of Physics.

natural ratio ($^{12}C:^{13}C = 1 - x:x$, where $x = 0.011$), to the almost pure ^{13}C ($x = 0.987$), the spectrum shifts towards longer wavelengths (see Figure 1.6) in good agreement with the expected $M^{-0.5}$ frequency dependence on the reduced mass M. For an approximately equal mix of the two isotopes, the authors reported that the features seen in the above two-phonon spectra were either broadened or unresolvable.

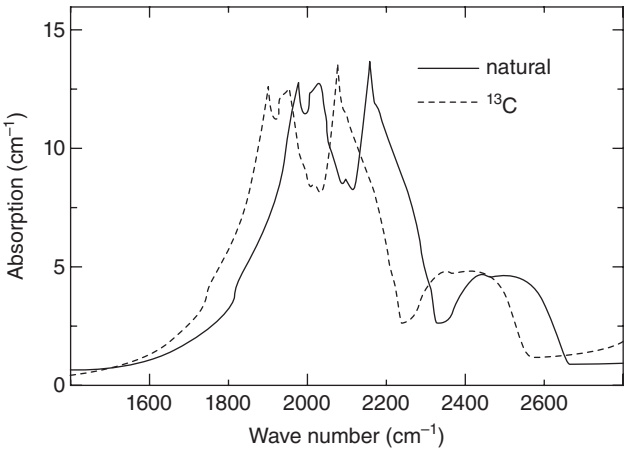

Figure 1.6 Two-phonon absorption spectra for enriched ^{13}C and natural isotopic fractions. Reproduced with permission from Ref. [7]; © 1998, American Physical Society.

1.3 UV Edge Absorption

The UV absorption edge begins for wavelengths slightly longer than the lowest energy bandgap at 227 nm (5.47 eV). The gap is indirect, and requires the excited electron to gain momentum in one of the <100> crystal directions. As a result, absorption near the UV edge is a three-body interaction, involving either the absorption or emission of a lattice phonon, and is weaker than would be the case for a direct bandgap. Close to the gap absorption is also influenced by interaction of the created electron and hole, which are weakly attractive (forming an exciton of binding energy $E_x = 0.07$ eV at room temperature), and which acts to slightly reduce the energy required to otherwise span the bandgap. A schematic diagram (Figure 1.7a) shows the indirect and direct bandgaps of diamond, along with the transitions involved in the near bandgap absorption.

A detailed description of the absorption edge (as shown in detail in Figure 1.7b) is given by Clark *et al.* [20]. At room temperature, the main onset of absorption occurs at 236 nm (labeled E_2 at 5.26 eV, 0.21 eV below the indirect bandgap energy E_g), and coincides with the excitation of an outer electron from the top of the valence band to the excitonic state just below the conduction band minimum and assisted by the absorption of a highest energy phonon. The conduction band minimum resides at a momentum value 76% of the Brillouin zone [21], where the highest energy phonon has energy of approximately 0.15 eV. For shorter wavelengths, absorption increases due to the increased density of states (which scales with $[\hbar c/\lambda - E_{th}]^{1/2}$, where E_{th} is the threshold energy for the phonon-assisted transition), and due to added contributions from the lower-energy transverse optical and

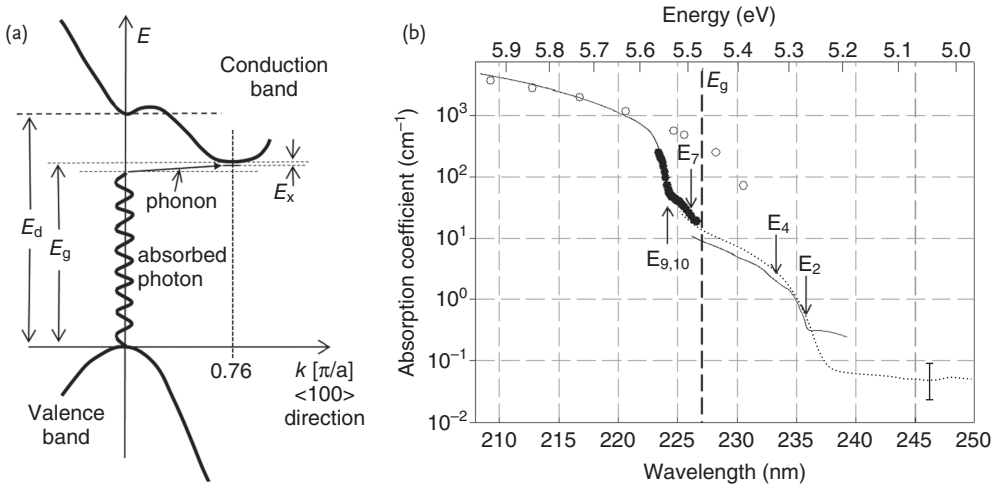

Figure 1.7 (a) Electronic band diagram highlighting the absorption mechanism for photon energies just below the bandgap. E_d and E_g are the direct and indirect band gaps, and E_x is the exciton binding energy; (b) The UV absorption edge at 295 K (solid lines, solid circles) [20]. The labels E_n, which retain the system of Ref. [20], show the features in the spectrum described in the text. The data of Philipp and Taft [19] (open circles) were determined from reflectance measurements. The dotted trace indicates the absorption coefficient determined from the transmission data for the Type IIa CVD sample of Figure 1.1.

acoustic phonon modes as the incident photon energy increases above their respective thresholds at 235.5 nm (5.27 eV) and 233.5 nm (E_4; 5.31 eV). For wavelengths shorter than 230.8 nm, the photon and phonon have sufficient energy to create an unbound electron–hole pair, and for such bound–unbound transitions the absorption increases according to $(\hbar c/\lambda - E_{th})^{3/2}$. Due to the low ambient density of high-energy phonons in diamond at room temperature, the absorption remains moderate until the photon energy exceeds the threshold for phonon emission. Evidence for phonon emission thresholds appears at 226 nm for the TA phonon (E_7; 5.482 eV), and at 224 nm for the closely spaced TO and longitudinal phonons (E_9; 5.531 eV and E_{10}; 5.544 eV, respectively). Transmission may be readily measured through thin samples up to the first direct band gap at $E_d = 7.3$ eV (170 nm), although at shorter wavelengths the absorption depth falls sharply and is limited to only a few microns of material. Absorption at wavelengths shorter than 200 nm has also been studied extensively (see e.g., Refs [19, 22]).

With increasing temperature, the absorption edge is influenced by the increased role of thermally excited phonons and the downshift in the phonon energy due to lattice expansion. The absorption spectra for a range of temperatures between 126 and 661 K are shown in Figure 1.8 [20]. The frequency downshift is small compared to the photon energy, and corresponds to less than 0.1 eV over the entire temperature range. The increasing absorption at wavelengths longer than 236 nm (<5.26 eV) for temperatures above 300 K is attributed to the increased density

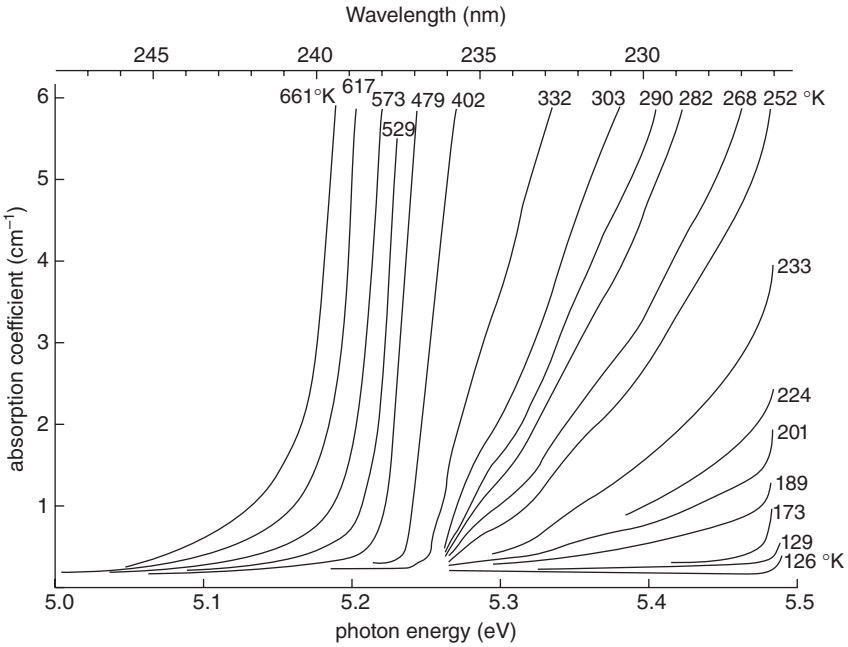

Figure 1.8 UV absorption edge as a function of temperature. The top wavelength scale has been added for convenience. Reproduced with permission from Ref. [20]; © 1964, Royal Society Publishing.

of thermal phonons and the onset of absorption events involving two or more phonons. Below room temperature, absorption relying on single-phonon absorption diminishes so that the absorption edge retreats progressively towards the 226 nm threshold (E_7; 5.482 eV) corresponding to phonon emission.

To date, the effect of isotopic composition on UV absorption edge does not appear to have been studied in great detail. For higher concentrations of ^{13}C, the lower phonon frequencies shift the E_i thresholds towards shorter wavelengths in the case of phonon absorption, and towards longer wavelengths in the case of phonon emission. In addition, the bandgap wavelength shifts due to the change in electron–phonon coupling for the heavier atomic constituents and a minor contribution (of approximately one-fourth) from the change in molar volume. For pure ^{13}C, the indirect bandgap increases by 13.6 meV, corresponding to a blue-shift of 0.56 nm [23].

1.4 Refractive Index

The refractive index values of Peter [24] and Edwards and Ochea [25] are plotted in Figure 1.9a (for an extended list of values, see Ref. [3] and page 670 in Ref. [2]).

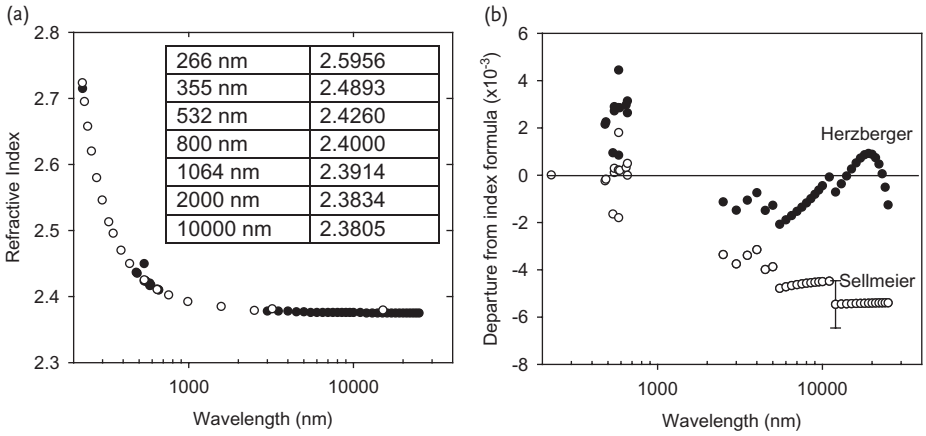

Figure 1.9 (a) Refractive index as a function of wavelength (hollow – [24], filled – [25] and references therein). The inset table contains Equation (1.6) values for several key wavelengths listed; (b) The departure of measured index values from the index formula.

Two common fits to the data are:

$$\text{Sellmeier [24]} \quad \boldsymbol{n}^2 = 1 + \frac{0.3306\lambda^2}{\lambda^2 - (175.0)^2} + \frac{4.3356\lambda^2}{\lambda^2 - (106.0)^2} \tag{1.5}$$

$$\text{Herzberger [2]} \quad n = A + \frac{B}{\dfrac{\lambda}{1000} - 0.028} + \frac{C}{\left(\dfrac{\lambda}{1000} - 0.028\right)^2} + D^2 + E^4 \tag{1.6}$$

where $A = 2.378\,37$, $B = 1.188\,97$, $C = -1.0083 \times 10^{-4}$, $D = -2.3676 \times 10^{-5}$, $E = 3.242\,63 \times 10^{-8}$, and where λ is in nanometers. Note that the coefficients for the Herzberger formula published earlier in Ref. [25] are in error. The two formulae provide slightly different fits to the data, with improved agreement for the visible and IR data respectively, as shown in Figure 1.9b. The shift in index with isotopic ratio has been estimated to be +0.0004 for ^{13}C in the long-wavelength limit ([26]; see also Refs [19] and [20]).

1.4.1
Temperature Dependence of the Refractive Index

The temperature dependence of n has been obtained using a number of methods, including electronic measurements of the dielectric coefficient and from the interference fringes in Fourier transform spectra for thin heated windows. Some results are summarized for measurements at several wavelengths in Figure 1.10a. By using the latter method, Ruf *et al.* [26] have measured the dependence at long wavelengths (100 μm), and have shown a good agreement with the empirical relationship

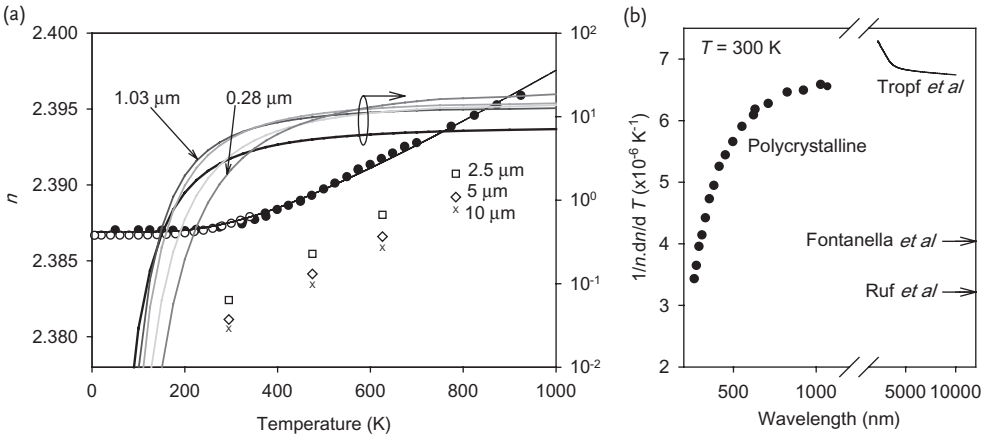

Figure 1.10 (a) Refractive index and thermo-optic coefficient versus temperature. Index data includes $\lambda = 100\,\mu m$ (solid circles [26]), $\lambda \rightarrow \infty$ (open circles [27]) and $\lambda = 2.5$, 5, and 10 μm [28]. The solid black curves for n and $1/n \times dn/dT$ are obtained using Equation (1.7). The colored curves correspond to Equation (1.7) using values ω_{eff} and K obtained for polycrystalline material at wavelengths 1.03, 0.62, 0.41, and 0.28 μm (brown, orange, light green, and dark green) [29]; (b) Values of $1/n \times dn/dT$ at 300 K as a function of wavelength [26–28]. The solid circles correspond to polycrystalline material [29]. For a color version of this figure, please see the color plate at the end of this book.

$$n(T) = n_0 + K\left[n_{BE}(\hbar\omega_{eff}, T) + \frac{1}{2}\right] \tag{1.7}$$

where $n_{BE}(\hbar\omega, T)$ is the Bose–Einstein factor of Equation (1.2) for an effective phonon frequency $\hbar\omega_{eff} = 711\,cm^{-1}$, and where $K = 0.019 \pm 0.007$. The index is found to remain constant at temperatures up to approximately 200 K, and increases linearly at temperatures above 450 K. The unusually high Debye temperature for diamond extends the range of constant index to notably higher temperatures compared to other materials. As a further consequence, the room temperature thermo-optic coefficient $(1/n) \times dn/dT$ is a steep function of temperature for diamond. Equation (1.7) describes the increase in vibrational degrees of freedom with temperature. An analysis of how the quantum and thermal motion affects the temperature dependence is presented in Refs [26, 30], although as with many other materials a comprehensive theory is yet to be developed.

The thermo-optic coefficient is also dependent on wavelength. The coefficient in the long-wavelength limit was determined from capacitive measurements for $T = 5.5$–340 K by Fontanella *et al.* [27] (open circles in Figure 1.10a), and at 100 μm by Ruf *et al.* (solid symbols), both of which are in good agreement. Fontanella *et al.* reported a slightly higher room-temperature value ($4.04 \times 10^{-6}\,K^{-1}$; cf. $3.2 \times 10^{-6}\,K^{-1}$ for Ruf *et al.*). Tropf *et al.* [28] have also reported a value of $6.7 \times 10^{-6}\,K^{-1}$

near 10 μm, although this was likely to be overvalued as it most likely presumed a linear dependence near room temperature [26].

Knowledge of the thermo-optic coefficient at shorter wavelengths is relatively poor, especially for single-crystal materials. Hu and Hess [29] used ellipsometry to study the refractive index at wavelengths spanning the near-IR to UV for nanocrystalline films grown by chemical vapor deposition. The results in Figure 1.10b show that the coefficient $(1/n) \times dn/dT$ decreases by as much as half of the long wavelength value for wavelengths approaching the bandgap. Comparisons of the Hu and Hess data with the aforementioned long-wavelength results of Ruf *et al.* and Fontanella *et al.* suggest that the Hu and Hess data are systematically overvalued; however, if the trend can be applied to bulk single crystal, then $(1/n) \times dn/dT$ values less than $2 \times 10^{-6}\,K^{-1}$ would be expected at wavelengths less than 400 nm.

1.5 Verdet Constant

The Faraday rotation of polarization was investigated for diamond by Ramaswasan [31]. The Verdet constant V, which is a function of material dispersion and thus wavelength, is related to the magnetic anomaly γ via the relationship:

$$V = \gamma \frac{e}{2m_e c^2} \lambda \frac{dn}{d\lambda} \tag{1.8}$$

where m_e and e are the electron mass and charge, respectively. Ramaswasan found that γ was constant at 27.8% in the visible, giving, for example, a value of V of approximately $6.8\,rad\,T^{-1}\,m^{-1}$ at 589 nm.

1.6 First-Order Raman Scattering

First-order Raman scattering results from the interaction of an incident electromagnetic photon with a near zero-wavevector optical phonon, which is the vibrational mode involving the relative movement of the two face-centered cubic lattices that comprise the diamond lattice in the direction of the linking carbon–carbon bond (see Figure 1.11a). At this point in the phonon dispersion curves, the longitudinal and two transverse vibrational branches converge and the Raman mode is triply degenerate. The Raman frequency ω_r is $1332.3\,cm^{-1}$ (or 39.99 THz) at room temperature.

The quantum mechanical theory of spontaneous Raman scattering in crystals has been reviewed by Loudon [32], in which diamond is used as a main example. The coupling between incident and output photons is mediated by a photon–electron interaction in which the incident photon deforms the periodic electron potential and induces a lattice phonon. For a polarized beam entering a crystal of

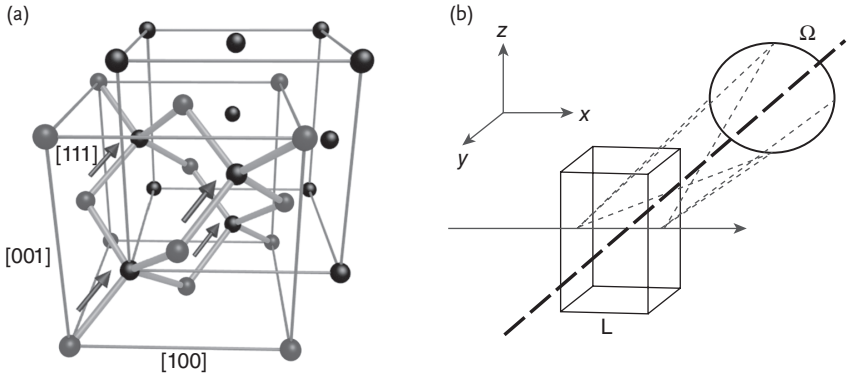

Figure 1.11 (a) The diamond lattice showing the two interpenetrating face-centered cubic lattices and the direction of relative movement for the zero wave-vector optical phonon involved in first-order Raman scattering; (b) Configuration for perpendicular Raman scattering. For a color version of this figure, please see the color plate at the end of this book.

length L, the fraction of photons scattered perpendicular to the incident beam into a detector of collection solid angle Ω is given by (see e.g., Refs [33, 34])

$$S = \frac{\hbar(2\pi)^4 N(n_{\mathrm{BE}}+1)\Omega L}{2\lambda_s^4 M\omega_r}\sum_j \left|\boldsymbol{e}_s R_j \boldsymbol{e}_i\right|^2 \tag{1.9}$$

where n_{BE} is the Bose–Einstein occupation number at ω_r, $N = 4/a_0{}^3$ is the number of unit cells, a_0 the lattice constant (8.81×10^{28} cells m^{-3} and 3.567 Å respectively at room temperature), $M = \rho/4N$ is the reduced mass of the carbon–carbon scattering center, and ρ is the crystal density (3.52 g cm^{-3}). Diamond's combination of high density, small mass and large deformation potential is responsible for a high scattering efficiency compared to other crystals. The efficiency for anti-Stokes scattering can be obtained using the same relation by replacing (n_{BE} + 1) with n_{BE}, and is typically 600 times weaker at room temperature. The Raman tensor R_j describes the strength of the interaction as a function of the incident and Stokes scattered polarizations e_{i} and e_{s} and with respect to each of the three degenerate Raman modes, $j = 1, 2$, and 3. The symmetry of the zone-center optical phonon (Γ_{25}+ in the notation of Birman, or equivalently F_{2g}) imposes the following form of R_j in the frame of the cubic axes $x = [100]$, $y = [010]$, and $z = [001]$:

$$R_1 = \begin{bmatrix} 0 & d & 0 \\ d & 0 & 0 \\ 0 & 0 & 0 \end{bmatrix} R_2 = \begin{bmatrix} 0 & 0 & 0 \\ 0 & 0 & d \\ 0 & d & 0 \end{bmatrix} R_3 = \begin{bmatrix} 0 & 0 & d \\ 0 & 0 & 0 \\ d & 0 & 0 \end{bmatrix} \tag{1.10}$$

where $d = \mathrm{d}\alpha/\mathrm{d}q$ is the change in crystal polarizability α with movement of the two sub-lattices along q, a characteristic of the material related to the lattice

deformation potentials. The Raman tensors for the common crystal orientations of $x' = [110]$, $y' = [1\bar{1}0]$, and $z' = [001]$, obtained by rotation of the coordinate system about 45° around the z-axis, are:

$$R_1 = \begin{bmatrix} \mathbf{0} & \mathbf{0} & \frac{d}{\sqrt{2}} \\ \mathbf{0} & 0 & \frac{d}{\sqrt{2}} \\ \frac{d}{\sqrt{2}} & \frac{d}{\sqrt{2}} & \mathbf{0} \end{bmatrix} R_2 = \begin{bmatrix} 0 & 0 & \frac{d}{\sqrt{2}} \\ 0 & 0 & -\frac{d}{\sqrt{2}} \\ \frac{d}{\sqrt{2}} & -\frac{d}{\sqrt{2}} & 0 \end{bmatrix} R_3 = \begin{bmatrix} d & \mathbf{0} & \mathbf{0} \\ 0 & -d & \mathbf{0} \\ \mathbf{0} & \mathbf{0} & \mathbf{0} \end{bmatrix} \tag{1.11}$$

The Raman tensors for the common crystal orientation of $x'' = [110]$, $y'' = [\bar{1}12]$, and $z'' = [1\bar{1}1]$, obtained by a rotation of arcos $[1/\sqrt{3}](\approx 54.7\,^\circ)$ around the x'-axis, are

$$R_1 = \begin{bmatrix} 0 & \frac{d}{\sqrt{3}} & \frac{d}{\sqrt{6}} \\ \frac{d}{\sqrt{3}} & \frac{2d}{3} & -\frac{d}{3\sqrt{2}} \\ \frac{d}{\sqrt{6}} & -\frac{d}{3\sqrt{2}} & -\frac{2d}{3} \end{bmatrix} R_2 = \begin{bmatrix} \mathbf{0} & \frac{d}{\sqrt{3}} & \frac{d}{\sqrt{6}} \\ \frac{d}{\sqrt{3}} & -\frac{2d}{\mathbf{3}} & \frac{d}{3\sqrt{2}} \\ \frac{d}{\sqrt{6}} & \frac{d}{3\sqrt{2}} & \frac{\mathbf{2}d}{\mathbf{3}} \end{bmatrix} R_3 = \begin{bmatrix} d & \mathbf{0} & \mathbf{0} \\ \mathbf{0} & -\frac{d}{3} & \frac{\sqrt{2}d}{\mathbf{3}} \\ \mathbf{0} & \frac{\sqrt{2}d}{3} & -\frac{\mathbf{2}d}{\mathbf{3}} \end{bmatrix} \tag{1.12}$$

It should be noted that the symmetric nature of R is only strictly valid for photon frequencies much larger than ω_r.

The absolute value of d, which is a function of wavelength, has been determined using a variety of methods, and ranges from 3.4 to $5.8 \times 10^{-16}\,\mathrm{cm}^2$ [35, 36] in the visible range. Owing again to the fact that diamond is often used as a simple and representative example for developing theory, the knowledge of the absolute value of the Raman tensor is better known compared to other materials, and often represents a reference for scattering intensity. Perhaps the most certain value is $|d| = 4.4 \pm 0.3 \times 10^{-16}\,\mathrm{cm}^2$ at 514.5 nm of Grimsditch and Ramdas [37], who developed a method based on the ratio of the Brillouin and Raman scattered intensities that avoids uncertainties introduced by absolute photometric measurements. Using this value of d, $S = 6.1 \times 10^{-7}$ for the case of y-polarized incident light for a cubic cut crystal in the configuration of Figure 1.11b (i.e., polarized along [010], in the plane including the incident beam and detector) and with $L = 1$ cm and $\Omega = 1$ srad. The scattered light is unpolarized, whereas for a z-polarized incident beam the scattering efficiency is half this value and polarized in the x-direction. The scattering efficiency as a function of incident polarization has been calculated using Equation (1.9) for the standard cases of perpendicular and axially directed scattering for a linearly polarized incident beam for input beams directed along the major crystallographic axes <100>, <110>, and <111>. The results, which represent the scattering behavior of any material with an F_{2g} Raman mode, are plotted in Figure 1.12 as functions of the incident and scattered polarization directions. The two scattering geometries discussed above correspond to Figure 1.12b with

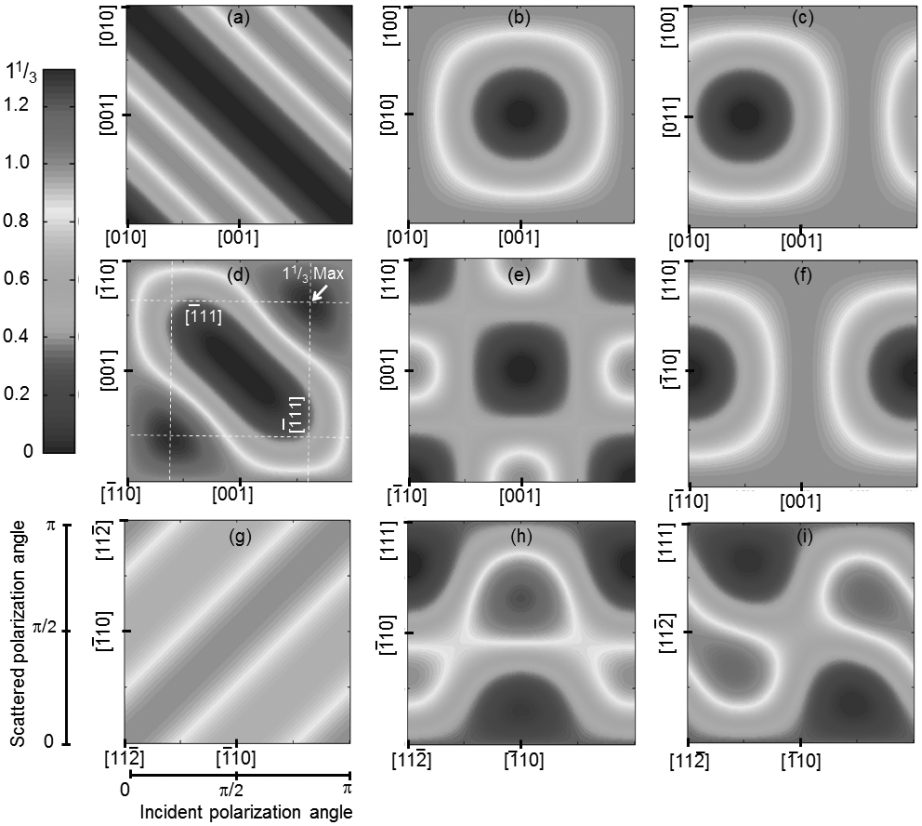

Figure 1.12 Scattering efficiency $\left(\sum_j |\boldsymbol{e}_s \boldsymbol{R}_j \boldsymbol{e}_i|^2\right) \Big/ d^2$ as a function of input and Stokes beam polarizations for several beam directions. (a–c) For an incident beam along a <100> axis for axially directed scattering, perpendicular scattering in direction <100>, and perpendicular scattering in the direction <110>, respectively; (d–f) For an incident beam along a <110> axis for axially directed scattering, perpendicular scattering in direction <110>, and perpendicular scattering in the direction <100>, respectively; (g–i) For an incident beam along a <111> axis for axially directed scattering, perpendicular scattering in direction <112>, and perpendicular scattering in the direction <110>, respectively. For a color version of this figure, please see the color plate at the end of this book.

input polarizations [010] and [001]. The highest value for the scattering matrix element is $4d^2/3$, which is obtained for light directed along the <110> direction for incident and scattered light polarized along the <111> direction (see Figure 1.12d). Polarized scattering data can be a useful aid for orienting diamond samples [38]. The effects of the surface, sample size and crystal imperfections have been reviewed in Ref. [39].

1.6.1
Wavelength Dependence

Efficiency increases at shorter wavelengths due to the characteristic λ^{-4} dependence for scattering, but is also enhanced by resonances between the sum and difference combinations of the pump, Stokes and Raman frequencies with transitions across the electronic bandgap. Figure 1.13a shows a comparison of $|d|$ as a function of the pump wavelength with other materials. The increase in $|d|$ at shorter wavelengths is attributed to resonance with the first direct bandgap [33]. By calculating the resonant contribution using a parabolic two-band model [33, 36],[3] a relation for the dispersion of gain was derived as:

$$|d| = 6.5 \times 10^{-16}\ g\,(\lambda_g/\lambda) \tag{1.13}$$

where d is in units of cm^2 and where

$$g(x) = x^{-2}[2-(1-x)^{-1/2}-(1+x)^{-1/2}] \tag{1.14}$$

takes into account the increase in density of states at shorter wavelengths. Here, λ is the pump wavelength and λ_g is taken as 207 nm (6 eV). Although measurements at short wavelengths are scarce, theoretical predictions suggest that the

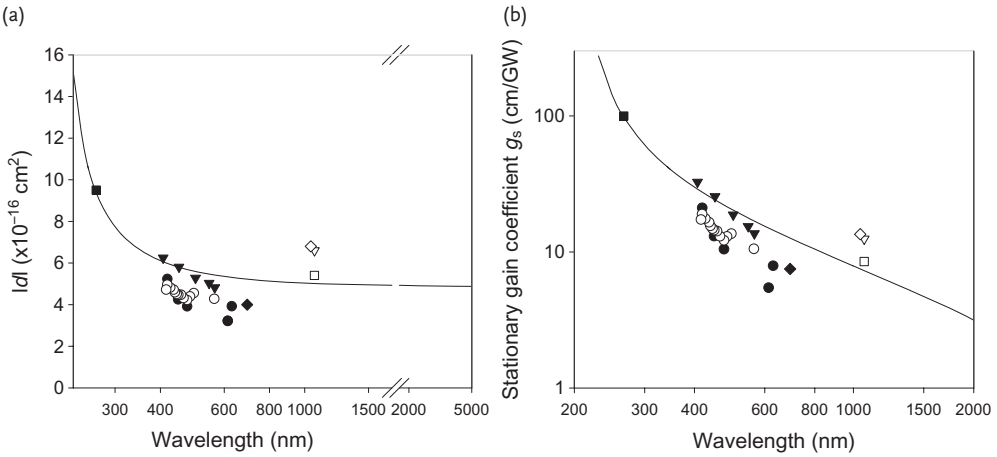

Figure 1.13 (a) $|d|$ and (b) g_s as a function of pump wavelength. Conversion between $|d|$ and g_s was performed where needed using Equation (1.20) with the Raman linewidth taken to be 1.5 cm^{-1} and $\sum_j |\boldsymbol{e}_s \boldsymbol{R}_j \boldsymbol{e}_i|^2 = d^2$. The data points are obtained from Refs [40] (closed squares), [36, 41] (solid triangles), [33] (solid and open circles), [42] (open triangle; see Section 8.2.1, open square), [43] (solid diamond), and [44] (open diamond). The curve in (a) was obtained using Equations (1.13) and (1.14), and in (b) using Equations (1.13), (1.14), and (1.20).

3) See the note added in proof in Ref. [33].

resonance for wavelengths approaching the bandgap is not as strong as for the Group IV analogs Si and Ge [35, 45].

1.6.2 Raman Linewidth

The finite linewidth of the Stokes shift, which is observed in the broadened frequency spectrum of the scattered light, results from anharmonic forces on the zone-center phonon oscillator and its resultant damping (with rate Γ) [46]. The full-width at half-maximum of the Lorentzian line shape $\Delta\nu = \Gamma/\pi c$ (in units of cm^{-1}) has been measured by several groups, with values ranging from 1 to 4 cm^{-1} at room temperature (see the recent study in Ref. [47] and references therein), most of which are based on direct measurements of the Raman spectrum. Determining accurate widths is not straightforward due to the compounding effects of instrument resolution and sample purity. The linewidth is of the order of the resolution of most conventional spectroscopic instruments (i.e., diffraction grating and Fourier transform IR spectrometers); thus, accurate measurements require detailed consideration of the instrument function. Liu *et al.* [48] aimed at carefully considering the spectrometer resolution and reported a room temperature value of approximately 1.2 cm^{-1}. By using a Fabry–Perot interferometer to analyze the broadened lineshape, McQuillan *et al.* [43] measured widths between 2.04 and 2.22 cm^{-1} for three Type IIa samples, with a quoted uncertainty of 0.04 cm^{-1}. Solin and Ramdas measured 1.65 ± 0.02 cm^{-1} [9]. Alternative methods based on ultrafast coherent phonon spectroscopy [47, 49], which measure the phonon damping rate using a pair of ultrafast pulses, yielded 1.5 ± 0.07 cm^{-1} and 1.54 ± 0.39 cm^{-1}. Levenson *et al.* [50] used a value of 1.02 cm^{-1} in order to fit the observed wavelength dependence of intensity of the coherent anti-Stokes Raman signal. As the damping rate measurements by ultrafast phonon spectroscopy are less affected by instrument functions, these values are expected to be more accurate. It is presently unclear how sample impurities and lattice defects may affect the Raman linewidth, however. Highly nitrogen-doped samples have been shown to introduce a small amount of broadening (from 1.54 to 1.81 cm^{-1} with up to 100 ppm of nitrogen) [49], variations in the nitrogen content may be responsible for the inconsistencies seen in measured values.

A linewidth of 1.5 cm^{-1} corresponds to a phonon dephasing time ($T_2 = 1/\Gamma$) of 7.1 ps and an oscillator quality factor ($T_2\omega_t$) of 1800. The main damping mechanism has been proposed to result from a resonant coupling with pairs of acoustic phonons of opposite momentum at the Raman frequency [51]. The dephasing time is shorter compared to the other Group IV crystals sharing a diamond lattice symmetry (Si, Ge, and Sn), and reflects a slightly higher density of states for the allowed two-phonon decay products [52]. It is also notably shorter than the strong 1047 cm^{-1} Raman mode of barium nitrate (T_2 = 20 ps at room temperature [53]), which is an outstanding example of a molecular crystal containing a phonon oscillator with very small anharmonic forces.

1.6.3 Temperature Dependence

Temperature influences the scattering efficiency, linewidth, and center frequency of Raman scattering. Observed ratios of the Stokes and anti-Stokes signals are consistent with the predicted temperature dependence resulting from n_{BE} in Equation (1.9) [54]. It is also found that as temperature is raised, the center frequency decreases and the linewidth broadens. The temperature dependence of the center frequency has been investigated by numerous groups, including a study conducted more than 60 years ago by Krishnan at temperatures up to 1000 K [55]. Data obtained from several of the more recent studies are shown in Figure 1.14a. Accurate determinations have been problematic due to difficulties in accurately recording the sample temperature and deconvolving the instrument function [58], and the absence of satisfactory *ab initio* theory to underpin the data [59]. The decrease in center frequency with temperature, which occurs primarily due to the change in force constants as the lattice expands, is described well by the semi-empirical relationship [58]:

$$\omega_r(T) = \omega_r(\mathbf{0}) - A \cdot n_{BE}(B \cdot \omega_r(T=0)) \tag{1.15}$$

where the Raman frequency at absolute zero is taken as $\omega_r(0) = 1332.7 \pm 0.2$ [48], and $A = 56 \pm 2$ and $B = 0.75 \pm 0.02$ are determined by fitting to data in Figure 1.14a. The results of the study in Ref. [48] suggest that B should be equal to 0.5, in accordance with a damped oscillator model based on two acoustic phonons of opposite momentum from the same branch (the Klemens model [51]); however, the agreement with experiment is less satisfactory when using this value.

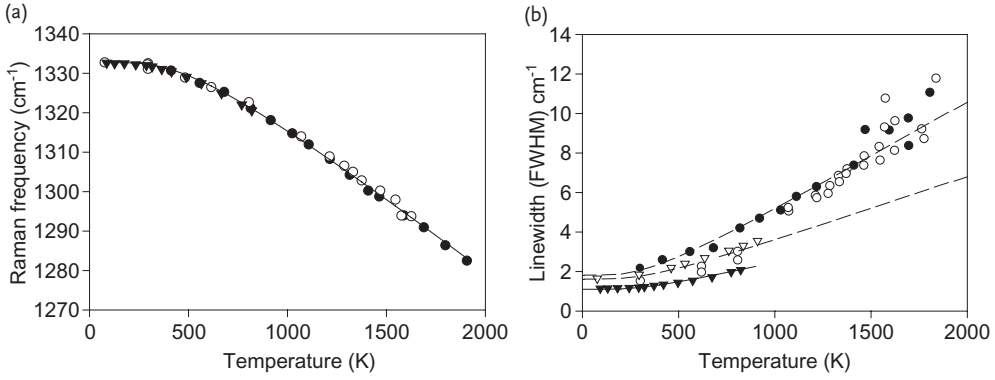

Figure 1.14 (a) Dependence of the first-order Stokes center frequency on temperature; (b) Dependence of Raman linewidth on temperature. The data are from Refs [56] (filled circles), [54] (open circles), [48] (filled triangles), and [57] (open triangles). In (b), the solid line corresponds to Equation (1.16) with $A' = 2$ and $B' = 0.5$ (Klemens model) and with $\Gamma(0) = 1.103\,\text{cm}^{-1}$. The dashed lines show how the parameters A' and B' may be varied in order to fit the data. The lower and upper curves $A' = 2$ and 3 respectively, both with $B' = 0.5$.

The linewidth is known with much less certainty, as highlighted by the spread of the selected data compiled in Figure 1.14b. The Klemens model has been proposed in many studies [48, 51, 56] as a good approximation in which the linewidth dependence is given by

$$\Delta n(T) = \Delta n(0) \cdot (1 + A' \cdot n_{\mathrm{BE}}(B' w_r[T = 0]) \tag{1.16}$$

where $A' = 2$ and $B' = 0.5$. Good agreement was obtained by Liu *et al.* [48], Borer *et al.* [57], and Herchen and Capelli [54] for T less than 1000 K. In order to fit the higher-temperature data of Zouboulis and Grimsditch [56] and Herchen and Capelli [54], a value of $A' \approx 3.0$ is required. The dashed curves in Figure 1.14b show Equation (1.16) for these two choices of A'. It is clear that accurate determinations of linewidth temperature dependence are challenging, and further investigations on this topic are required to fully test the validity of the Klemens model.

1.6.4
Isotopic Content

The dependence of the center frequency and lineshape with isotopic content has been investigated in several studies [60–63]. The Raman spectrum for extreme and intermediate concentrations of ^{12}C and ^{13}C is shown in Figure 1.15a. From $\omega_r = 1332.4\,\mathrm{cm}^{-1}$ for natural diamond (^{13}C fraction $x = 0.011$), the measured room-temperature center frequency increases to $1332.7\,\mathrm{cm}^{-1}$ for $x = 0.001$, and decreases to $1282\,\mathrm{cm}^{-1}$ for a highly enriched ^{13}C ($x = 0.99$) [63]. Based on these measure-

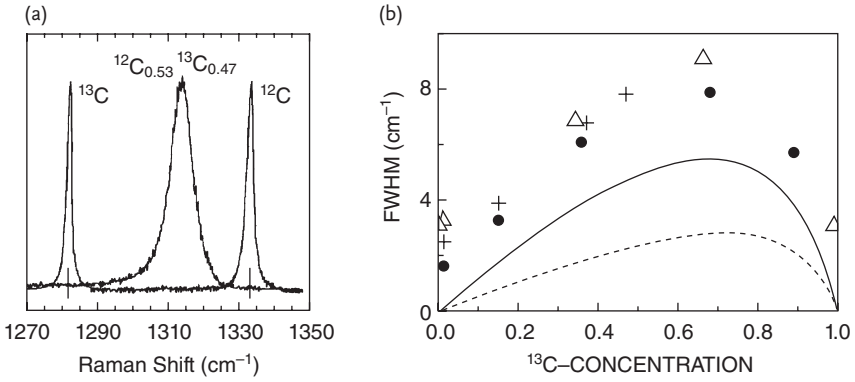

Figure 1.15 (a) The Raman line shape for several alloy fractions. Figure reproduced with permission from Ref. [60]; © 2001, Elsevier; (b) The full-width half-maximum as a function of the isotopic fraction. Figure reproduced with permission from Ref. [62]; © 1993, Elsevier. As detailed in the reference, the symbols correspond to data compiled from several studies, and the two curves show model results obtained using differing assumptions for the density of states.

ments and those of Ref. [61], the following polynomial was used to fit the room-temperature data:

$$\omega_r(x) = 1332.82 - 34.77x - 16.98x^2 \tag{1.17}$$

The frequency shift is explained by two contributions affecting the Raman frequency: one involving the change in average mass proportional to $M_{av}{}^{-0.5}$ where $M_{av} = (1-x)M_{12} + xM_{13}$; and the other involving the random distribution of isotopes in the bulk referred to as "isotopic disorder," which is responsible for a small frequency increase. A thorough theoretical treatment involves consideration of the disorder-induced anharmonic terms, as well as contributions arising from a relaxation in the requirement for wavevector conservation due to breakdown in the lattice translational invariance [60–63].

The shape and width are also found to vary significantly with x. The width as a function of isotopic ratio is shown in Figure 1.15b [62]. The notably larger values for the natural isotope ratio compared to the measurements of others (see Figure 1.14b) is not explained by the authors, but may be a result of a lower instrument resolution or by sample impurities. The ratio of ^{12}C and ^{13}C widths is slightly greater than unity consistent with the expected ratio of $M_{13}/M_{12} = 1.08$ [60]. For alloys, the width increases notably and the shape is no longer purely Lorentzian. This is highlighted by the spectrum for $x = 0.47$ in Figure 1.15a, which shows an extended shoulder on the low mass side and a linewidth of approximately 6 cm^{-1}. Explanation of the observed change in shape requires consideration of disorder-induced additional damping of the zone center phonon (which is sensitive to the precise form of the phonon dispersion curves near the Raman frequency) and the relaxation of wave-vector conservation [60–62]. The maximum width of approximately 8 cm^{-1} is otained near $x = 0.7$.

1.7 Stimulated Raman Scattering

Stimulated Raman scattering, in which growth in a Stokes field results from parametric coupling with the pump and phonon fields, was first observed in solids in a study involving diamond [64]. For the simple case of a plane wave pump pulse of duration much longer than T_2 and intensity I_p, the growth in the Stokes intensity in the z-direction is (refer also to Section 8.1.1.1)

$$dI_s/I_s = g_s I_p(z) \cdot dz \tag{1.18}$$

The gain coefficient g_s factors in the accumulated density of phonons (which decay on the order of T_2), and can be derived from the spontaneous Raman scattering values of d and Γ described above, using the relationship for the steady-state gain coefficient [65]

$$g_s(\omega_s) = \frac{4\pi^2\omega_s N}{n_s n_l c^2 M \omega_r} \frac{\Gamma}{(\omega_s - \omega_l + \omega_r)^2 + \Gamma^2} \sum_j \left| e_s R_j e_i \right|^2 \tag{1.19}$$

which, at the Stokes frequency line center, reduces to

$$g_s = \frac{4\pi^2 \omega_s N}{n_s n_l c^2 M \omega_r \Gamma} \sum_j \left| \boldsymbol{e}_s R_j \boldsymbol{e}_i \right|^2 \tag{1.20}$$

where ω_l and ω_s are the pump and Stokes frequencies, respectively, and n_l and n_s are the corresponding refractive indices. The gain coefficient is related to the imaginary part of the Raman susceptibility χ_R through

$$\chi_R = -n_s n_l g_s / 2\mu_0 \omega_s \tag{1.21}$$

Direct measurements of g_s have been made from the threshold for stimulated Raman scattering or by using pump–probe measurements. For single-pass stimulated Raman scattering of an intense pump beam, the pump intensity I_{th} threshold is conventionally obtained using the relationship

$$g_s = 25/L \cdot I_{th} \tag{1.22}$$

where it is assumed that the pump intensity is maintained over L and that a gain factor of e^{25} marks the onset of observable stimulated Raman scattering. In the presence of a Stokes resonator, the gain can be determined by equating the steady-state gain with the resonator losses at threshold. Since gain depends on intensity, a good knowledge of the beam diameters and beam shape is required. A more detailed review of g_s values is given in the context diamond Raman lasers in Chapter 8.

Gain coefficient values have been determined for pump wavelengths between 266 nm and 1064 nm, as shown in Figure 1.13b. For pumping at 1064 nm, the gain varies from more than 12.5 cm GW^{-1} for propagation along a <100> axis as determined from a measurement of SRS threshold [42], to 8.5 cm GW^{-1} using pump-probe techniques (see Section 8.2.1). The theoretical curve shows the expected wavelength dependence using Equation (1.20) and the semi-empirical expression for d (Equations 1.13 and 1.14) under the assumption that the linewidth is 1.5 cm^{-1} (T_2 = 7.1 ps). It is also assumed that a configuration is used in which $\sum_j \left| \boldsymbol{e}_s \boldsymbol{R}_j \boldsymbol{e}_i \right|^2 = d^2$, which is the case, for example, for co-propagating pump and Stokes beams along the <100> direction. Thus, a 33% enhancement may be obtained for the pump and Stokes polarization parallel to <111> axes (refer to Section 1.6). At long wavelengths, the gain is linear with Stokes frequency. It should be noted, however, that the above theory is only valid for Stokes frequencies much greater than ω_r which, for diamond, corresponds to $\lambda_s \ll 7.5\,\mu$m.

1.8 Brillouin Scattering

The wavelength shift and intensity of Brillouin scattering is determined by the elastic strain and photoelastic tensors, which for the cubic symmetry of diamond

Table 1.2 Elastic strain c_{ij} and photoelastic tensor p_{ij} elements [37]. For a discussion on the accuracy of the p_{ij}, see values in Ref. [66]. For reference, the dispersion of the p_{ij} has been considered in Ref. [67] (see also Ref. [3]), and the temperature and isotopic variation in the elastic strain is considered in Refs [68] and [69].

c_{11} (10^{11} Pa)	c_{12} (10^{11} Pa)	c_{44} (10^{11} Pa)	p_{11}	p_{12}	p_{44}
10.764	1.252	5.744	–0.249	0.043	–0.172

is characterized by the three pairs of parameters c_{11}, c_{12}, and c_{44}, and p_{11}, p_{12}, and p_{44}. Experimentally derived values for these are listed in Table 1.2.

The frequency shift is given by

$$\Delta\omega = \pm 2\omega_i n(v_s/c)\sin(\theta/2) \tag{1.23}$$

where θ is the angle between the incident and scattered radiation from the acoustic wave directed at the intermediate angle and n is the refractive index at ω. The speed of the longitudinal or transverse acoustic phonon $v_s = (X_q/\rho)^{0.5}$ can be determined from the appropriate combination of elastic strain tensor elements X_q. For phonons propagating along a cubic axis, for example, $X_q = c_{11}$ or c_{44} for longitudinal or transverse polarization respectively, giving $v_s = 1.8 \times 10^4\,\mathrm{ms}^{-1}$ and $1.3 \times 10^4\,\mathrm{ms}^{-1}$. For Brillouin scattering at visible wavelengths, the typical shift for perpendicular scattering from longitudinal acoustic phonons is 3.5–4.5 cm^{-1} and 2–3 cm^{-1} for transverse phonons.

The scattering efficiency at the Stokes wavelength can be calculated using [37, 70]

$$S = \frac{k_B T \omega_s^4 n^8 \Omega L}{128\pi^2 c^4} \frac{\sum_j \left(\boldsymbol{e}_s T_j \boldsymbol{e}_i\right)^2}{X_q} \tag{1.24}$$

where the sum is over the longitudinal and transverse acoustic waves and the T_j are the scattering tensors. For $k_B T$ much greater than acoustic phonon energy $\hbar\Delta\omega$, which is the case at room temperature, the intensity of Stokes and anti-Stokes are equal. For incident and scattered beams directed along perpendicular <110> axes, the relevant scattering tensors for the <100> directed longitudinal phonon and two degenerate transverse phonons are

$$T_1 = 2\begin{bmatrix} p_{11} & 0 & 0 \\ 0 & p_{12} & 0 \\ 0 & 0 & p_{12} \end{bmatrix} T_2 = 2\begin{bmatrix} 0 & p_{44} & 0 \\ p_{44} & 0 & 0 \\ 0 & 0 & 0 \end{bmatrix} T_3 = 2\begin{bmatrix} 0 & 0 & p_{44} \\ 0 & 0 & 0 \\ p_{44} & 0 & 0 \end{bmatrix} \tag{1.25}$$

Further, if the light beams are polarized normal to the scattering plane, $\sum_j \left(\boldsymbol{e}_s T_j \boldsymbol{e}_i\right)^2 = 4p_{12}^2$ and $X_q = c_{11}$ so that the Brillouin scattering efficiency per unit solid angle S/Ω is approximately $10^{-8}\,\mathrm{srad}^{-1}$ at 500 nm for $L = 1$ cm. In this case, generated phonons are longitudinally polarized in the <100> direction. Scattering tensors and X_q values are listed in Ref. [37] for phonons directed along the symmetry directions <110> and <111>.

For stimulated Brillouin scattering, the steady-state gain coefficient at line center is given by [71]

$$g_B = n^7 \omega_s^2 p^2 / \rho v_s c^3 \Gamma_B \tag{1.26}$$

where p is the appropriate photoelastic tensor component. The damping of the acoustic wave Γ_B, has not been investigated in detail for diamond. According to Boyd [71], the damping rate of the scattering phonons or Brillouin scattering linewidth for materials is

$$\Gamma_B = q^2 / \rho [4/3\eta_s + \eta_b + k(C_p/C_v - 1)/C_p] \tag{1.27}$$

where q is the acoustic phonon wave-vector, η_s is the shear viscosity, η_b is the bulk viscosity, κ is the thermal conductivity and C_p and C_v are the specific heats at constant pressure and volume. The author is unaware of published η_s and η_v values, or measurements of acoustic phonon lifetime values. If, instead, the damping rate for Ge of $\Gamma_B = 1\,\mathrm{ns}^{-1}$ (from Ref. [72] and scaled for visible wavelengths $\omega_s \approx 4 \times 15\,\mathrm{rad\,s}^{-1}$) is used, then $g_B \approx 1.3\,\mathrm{cm\,GW}^{-1}$. Thus, pulse intensities of approximately $1\,\mathrm{GW\,cm}^{-2}$ with temporal coherence longer than 1 ns are expected to be necessary to achieve significant gain in crystals of length 1 cm long. To the present author's knowledge, no details of stimulated Brillouin scattering in diamond have yet been reported.

1.9 Electronic Nonlinearity

The third-order electronic nonlinearity $\chi^{(3)}$ results from a deformation of the lattice electron cloud at high incident electric field intensities, and is responsible for a wide range of fast (10^{-16} s) optical effects in the transparent region. These include four-wave mixing, third-harmonic generation, self-focusing (intensity-dependent refractive index), DC and optical Kerr effects, and multi-photon absorption. Direct measurements of the $\chi^{(3)}$ have been determined from experiments in four-wave mixing [41, 50], self-focusing ("Z-scan technique") [73], and the DC Kerr effect [74]. Values for the three independent tensor coefficients that characterize cubic crystals are listed in Table 1.3, and plotted as a function of wavelength in Figure 1.16 [75]. The fact that $\chi^{(3)}_{1111} = 3\chi^{(3)}_{1221} = 3\chi^{(3)}_{1122}$ holds approximately for diamond indicates that the electronic orbitals responsible for the nonlinearity are spherical on average, and that the electronic linearity is thus approximately directionally independent [41]. The magnitude is in general agreement with theoretical calculations based on the band structure [76], and is approximately one-twentieth of the real part of the resonant Raman nonlinearity. The magnitude is similar to lead silicate glasses, but notably lower compared to other crystals of similar refractive index. The wavelength dependence has not been modeled in detail for wide indirect bandgap materials such as diamond; however, general models for the nonlinear absorption [77] combined with a Kramers–Kronig analysis [73] seem to be useful in qualitatively predicting the wavelength dependence.

Table 1.3 The measured third-order susceptibility tensor components χ_{ijkl} and the nonlinear refractive index n_2. $\chi^{(3)}$ is related to the nonlinear polarization $P_i^{(3)}$ through $P_i^{(3)} = \varepsilon_0 \chi_{ijkl}^{(3)} E_j \cdot E_k \cdot E_l$. Note that the values reported in Ref. [41] have been increased by a factor of 4 to conform to the definition of the susceptibility used here, and in the convention of most other studies. The $\chi^{(3)}$ values in italics are calculated from n_2 measurements (and vice versa), as described in Section 1.9.1.

Wavelength (nm)	$\chi_{1111}^{(3)}$	$\chi_{1221}^{(3)}$	$\chi_{1122}^{(3)}$	n_2 (10^{-20} m^2 W^{-1})	Reference
	(10^{-21} m^2 V^{-2})				
530[a)]	3.2			*15.6*	[50]
545[a)]	2.6	0.96	1.02	*12.6*	[41]
565[a)]		0.88		12.8[b)]	[41]
450[a)]		1.22		17.8[b)]	[41]
407[a)]		1.46		21.3[b)]	[41]
650		0.217		*3.17*	[74]
532	*1.44*			7.0	[73]
355	*−2.76*			−13.4	[73]
1064	*0.864*			4.2	[73]
532	*1.44*			7.0	[73]
355	*−2.47*			−12	[73]
266	*−6.99*			−34	[73]

a) The wavelengths listed for the four-wave mixing experiments represent the pump beam wavelength.
b) Calculated using Equation (1.28) and assuming $\chi_{1122}^{(3)} = 3\chi_{1221}^{(3)}$.

The data indicate that $\chi_{1111}^{(3)}$ is approximately $1–3 \times 10^{-21}$ m^2 V^{-2} in the visible range, and increases slightly for shorter wavelengths approaching the threshold for two-photon absorption ($\lambda < 450$ nm). Values determined using "Z-scan" measurements of the nonlinear refractive index (see Section 1.9.1) indicate a change in sign at a wavelength approximately 70% of the bandgap (ca. 400 nm) and a significant increase in magnitude as the bandgap is approached. This behavior is characteristic of many other semiconductors. A model including the various contributions to the nonlinearity was developed in Ref. [78], which assumed a simple two-band structure (valence and conduction bands) and neglected the role of free carriers generated by two-photon absorption. This model was successful in reproducing the behavior of a large number of semiconductors, and suggests that the effects of two-photon absorption dominates the $\chi_{ijkl}^{(3)}$ wavelength dependence as the bandgap is approached. For photon energies much smaller than the bandgap, no significant dispersion is expected, as is confirmed by the data for wavelengths longer than 600 nm.

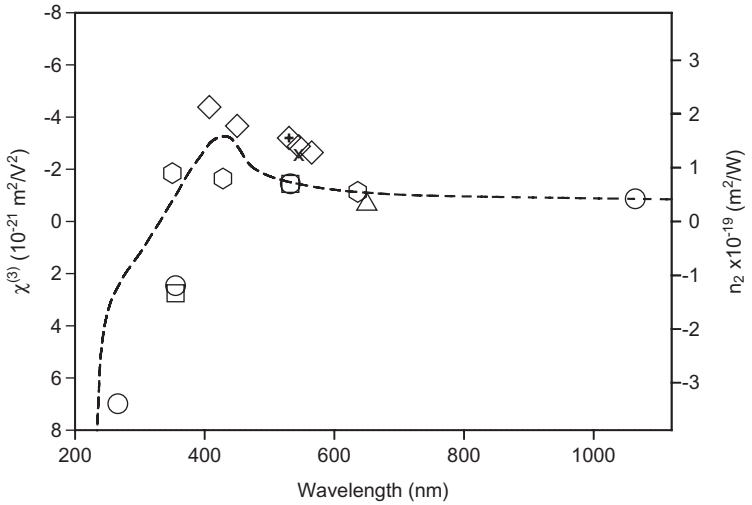

Figure 1.16 The dependence of susceptibility $\chi^{(3)}_{1111}$ on wavelength. Data are from Refs [50] (diamond with center cross), [73] (circles and squares), [74] (upward triangle), and [75] (hexagons). The hollow diamonds and (x) correspond to $3\chi^{(3)}_{1221}$ and $\chi^{(3)}_{1111}$ of Ref. [41]. The right-hand axis shows the nonlinear refractive index n_2 calculated from $\chi^{(3)}_{1111}$ using Equation (1.28). The dashed line is the theoretical wavelength dependence for n_2 obtained by a Kramers–Kronig analysis of the nonlinear absorption, as described in Ref. [73].

1.9.1
Nonlinear Refractive Index

The nonlinear refractive index arising from the nonresonant electronic nonlinearity can be measured directly using the Z-scan technique [73], and is related to $\chi^{(3)}_{ijkl}$ by [71]

$$n_2 = 3\chi^{(3)}_{1111}/4cn_0^2\varepsilon_0 \tag{1.28}$$

where n_2 is defined as the index change $n_2 I$ from the linearly polarized incident beam of intensity I. The results are included in Table 1.3 and Figure 1.16. In the visible range, n_2 is approximately $1\text{–}2 \times 10^{-19}\,m^2\,W^{-1}$. As for $\chi^{(3)}_{1111}$, n_2 changes sign at a wavelength of approximately 400 nm.

1.9.2
Two-Photon Absorption

Two-photon absorption coefficients β_2 for materials are known to scale reasonably well with the inverse fourth power of the band gap [77, 79]. Consequently, the two-photon absorption coeffiecient in diamond is relatively small compared to

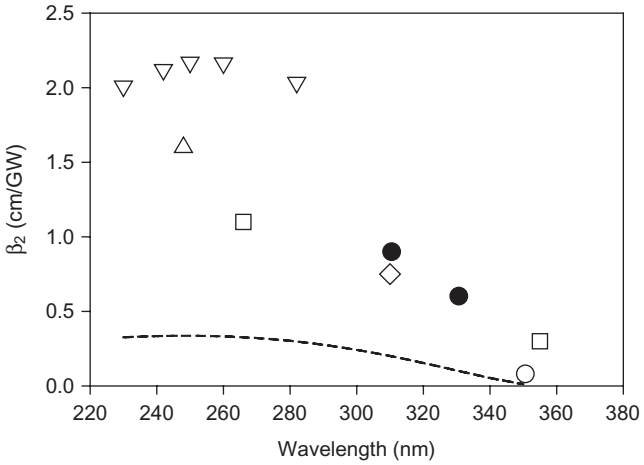

Figure 1.17 The dependence of β_2 on wavelength from solid circles [75], downward triangles [81], upward triangle [80], and squares [73]. The dashed line is the theoretical wavelength dependence of Ref. [79], assuming a direct bandgap energy of 7.0 eV.

that of most other semiconductors. The β_2 values are determined by measurement of the decrease in transmission as a function of the incident intensity. A summary of reported measurements is shown in Figure 1.17; also shown is the theoretical scaling formula of Van Stryland *et al.* [79], which has been used with good success to predict β_2 dispersion for direct bandgap semiconductors. Clearly, the measured β_2 values for indirect-bandgap diamond are notably larger than predicted by theory, although the general shape as a function of wavelength is in reasonable agreement. Although other models for two-photon absorption in diamond have been suggested [75, 81], to the present author's knowledge a comprehensive theory for the observed magnitudes and dispersion is yet to be reported. Three-photon absorption measurements have been recently reported in the range of 350 to 430 nm [75].

Acknowledgments

The author is grateful to Alex Sabella for his advice on Raman gain measurements, and to Andrew Lehmann and Ondrej Kitzler for assistance in preparing some of the figures. Thanks also to Brian Orr, David Coutts, Gerald Bonner, David Spence, and Marcos Grimsditch for useful comments on the manuscript. This material is partly based on research sponsored by the Australian Research Council Future Fellowship Scheme (FT0990622), and the Air Force Research Laboratory under agreement numbers AOARD-10-4078 and 12-4055.

References

1 Walker, J. (1979) Optical absorption and luminescence in diamond. *Rep. Prog. Phys.*, **42** (10), 1605.

2 Edwards, D. and Philipp, H.R. (1985) Cubic carbon (diamond), in *Handbook of Optical Constants of Solids* (ed. E.D. Palik), Academic Press, Orlando, FL, pp. 665–673.

3 Zaitsev, A.M. (2001) *Optical Properties of Diamond: A Data Handbook*, Springer, Berlin.

4 Smith, H.M.J. (1948) The theory of the vibrations and the Raman spectrum of the diamond lattice. *Philos. Trans. R. Soc. Lond. Ser. A Math. Phys. Sci.*, **241** (829), 105–145.

5 Lax, M. and Burstein, E. (1955) Infrared lattice absorption in ionic and homopolar crystals. *Phys. Rev.*, **97** (1), 39–52.

6 Thomas, M. (1994) Multiphonon model for absorption in diamond. *Proc. SPIE*, **2286**, 152.

7 Vogelgesang, R., Alvarenga, A.D., Hyunjung, K., Ramdas, A.K., Rodriguez, S., Grimsditch, M., and Anthony, T.R. (1998) Multiphonon Raman and infrared spectra of isotopically controlled diamond. *Phys. Rev. B*, **58** (9), 5408–5416.

8 Klein, C.A., Hartnett, T.M., and Robinson, J. (1992) Critical point phonon frequencies of diamond. *Phys. Rev. B*, **45** (22), 854–863.

9 Solin, S. and Ramdas, A. (1970) Raman spectrum of diamond. *Phys. Rev. B*, **1** (4), 1687–1698.

10 Wehner, R., Borik, H., Kress, W., Goodwin, A., and Smith, S. (1967) Lattice dynamics and infra-red absorption of diamond. *Solid State Commun.*, **5** (4), 307–309.

11 Mollart, T.P., Lewis, K.L., Pickles, C.S.J., and Wort, C.J.H. (2003) Factors affecting the optical performance of CVD diamond infrared optics. *Semicond. Sci. Technol.*, **18** (3), S117.

12 Harris, D. (1994) Properties of diamond for window and dome applications. *Proc. SPIE*, **2286**, 218–228.

13 Sussmann, R.S., Brandon, J.R., Coe, S.E., Pickles, C.S.J., Sweeney, C.G., Wasenczuk, A., Wort, C.J.H., and Dodge, C.N. (1998) CVD diamond: a new engineering material for thermal, dielectric and optical applications. *Ind. Diam. Rev.*, **3**, 69–77.

14 Sussmann, R.S., Pickles, C.S.J., Brandon, J.R., Wort, C.J.H., Coe, S.E., Wasenczuk, A., Dodge, C.N., Beale, A.C., Krehan, A.J., Dore, P., Nucara, A., and Calvani, P. (1998) CVD diamond windows for infrared synchrotron applications. *Il Nuovo Cimento D*, **20** (4), 503–525.

15 Lax, M. (1958) Optical properties of diamond type crystals. *Phys. Rev. Lett.*, **1** (4), 131–132.

16 Hahn, D.V., Thomas, M.E., Blodgett, D.W., and Kaplan, S.G. (2003) Characterization and modeling of the infrared properties of diamond and SiC. *Proc. SPIE*, **5078**, 148–158.

17 Piccirillo, C., Davies, G., Mainwood, A., and Penchina, C. (2001) The variation of optical absorption of CVD diamond as a function of temperature. *Phys. B Condens. Matter*, **308–310**, 581–584.

18 Piccirillo, C., Davies, G., Mainwood, A., Scarle, S., Penchina, C.M., Mollart, T.P., Lewis, K.L., Nesládek, M., Remes, Z., and Pickles, C.S.J. (2002) Temperature dependence of intrinsic infrared absorption in natural and chemical-vapor deposited diamond. *J. Appl. Phys.*, **92** (2), 756.

19 Philipp, H. and Taft, E. (1964) Kramers–Kronig analysis of reflectance data for diamond. *Phys. Rev.*, **136** (5A), 1445–1448.

20 Clark, C.D., Dean, P.J., and Harris, P.V. (1964) Intrinsic edge absorption in diamond. *Proc. R. Soc. A Math. Phys. Eng. Sci.*, **277** (1370), 312–329.

21 Dean, P., Lightowlers, E., and Wight, D. (1965) Intrinsic and extrinsic recombination radiation from natural and synthetic aluminum-doped diamond. *Phys. Rev.*, **140** (1), A352–A386.

22 Roberts, R. and Walker, W. (1967) Optical study of the electronic structure of diamond. *Phys. Rev.*, **161** (3), 730–735.

23 Collins, A.T., Lawson, S.C., Davies, G., and Kanda, H. (1990) Indirect energy gap

of ^{13}C diamond. *Phys. Rev. Lett.*, **65** (7), 891–894.
24 Peter, F. (1923) Uber brechungsindizes und absorptionkonstanten des Diamanten zwischen 644 und 226 mμ. *Z. Phys. A Hadrons Nucl.*, **15** (1), 358–368.
25 Edwards, D.F. and Ochoa, E. (1981) Infrared refractive index of diamond. *J. Opt. Soc. Am.*, **71** (5), 607–608.
26 Ruf, T. and Cardona, M. (2000) Temperature dependence of the refractive index of diamond up to 925 K. *Phys. Rev. B*, **62** (24), 16578–16581.
27 Fontanella, J., Johnston, R.L., Colwell, J.H., and Andeen, C. (1977) Temperature and pressure variation of the refractive index of diamond. *Appl. Opt.*, **16** (11), 2949–2951.
28 Tropf, W.J., Thomas, M.E., and Linevsky, M.J. (1998) Infrared refractive indices and thermo-optic coefficients for several materials. *Proc. SPIE*, **3425**, 160.
29 Hu, Z.G. and Hess, P. (2006) Optical constants and thermo-optic coefficients of nanocrystalline diamond films at 30–500 °C. *Appl. Phys. Lett.*, **89** (8), 1906–1906.
30 Karch, K., Dietrich, T., Windl, W., Pavone, P., Mayer, A., and Strauch, D. (1996) Contribution of quantum and thermal fluctuations to the elastic moduli and dielectric constants of covalent semiconductors. *Phys. Rev. B*, **53** (11), 7259–7266.
31 Ramaseshan, S. (1946) The Faraday effect in diamond. *Proc. Math. Sci.*, **24** (1), 104–113.
32 Loudon, R. (1964) The Raman effect in crystals. *Adv. Phys.*, **13** (52), 423–482.
33 Grimsditch, M., Cardona, M., Calleja, J.M., and Meseguer, F. (2005) Resonance in the Raman scattering of CaF_2, SrF_2, BaF_2 and diamond. *J. Raman Spectrosc.*, **10** (1), 77–81.
34 Anastassakis, E., Iwasa, S., and Burstein, E. (1966) Electric-field-induced infrared absorption in diamond. *Phys. Rev. Lett.*, **17** (20), 1051–1054.
35 Calleja, J., Kuhl, J., and Cardona, M. (1978) Resonant Raman scattering in diamond. *Phys. Rev. B*, **17** (2), 876–883.
36 Cardona, M. (1982) Resonance phenomena, in *Light Scattering Solids II* (eds M. Cardona and G. Guntherodt), Springer, Berlin, pp. 19–178.
37 Grimsditch, M. and Ramdas, A.K. (1975) Brillouin scattering in diamond. *Phys. Rev. B*, **11** (8), 3139–3148.
38 Mossbrucker, J. and Grotjohn, T.A. (1996) Determination of local crystal orientation of diamond using polarized Raman spectra. *Diamond Relat. Mater.*, **5** (11), 1333–1343.
39 (a) Prawer, S., Nugent, K.W., Jamieson, D.N., Orwa, J.O., Bursill, L.A., and Peng, J.L. (2000) The Raman spectrum of nanocrystalline diamond. *Chem. Phys. Lett.*, **332** (1-2), 93–97; (b) Prawer, S. and Nemanich, R.J. (2004) Raman spectroscopy of diamond and doped diamond. *Philos. Trans. Ser. A Math. Phys. Eng. Sci.*, **362** (1824), 2537–2565.
40 Granados, E., Spence, D.J., and Mildren, R.P. (2011) Deep ultraviolet diamond Raman laser. *Opt. Express*, **19** (11), 10857–10863.
41 Levenson, M. and Bloembergen, N. (1974) Dispersion of the nonlinear optical susceptibility tensor in centrosymmetric media. *Phys. Rev. B*, **10** (10), 4447–4463.
42 Kaminskii, A.A., Hemley, R.J., Lai, J., Yan, C.S., Mao, H.K., Ralchenko, V.G., Eichler, H.J., and Rhee, H. (2007) High-order stimulated Raman scattering in CVD single crystal diamond. *Laser Phys. Lett.*, **4** (5), 350–353.
43 McQuillan, A., Clements, W., and Stoicheff, B. (1970) Stimulated Raman emission in diamond: spectrum, gain, and angular distribution of intensity. *Phys. Rev. A*, **1** (3), 628–635.
44 Feve, J.-P.M., Shortoff, K.E., Bohn, M.J., and Brasseur, J.K. (2011) High average power diamond Raman laser. *Opt. Express*, **19** (2), 913–922.
45 Swanson, L. and Maradudin, A. (1970) Pseudopotential calculation of the Raman tensor for homopolar semiconductors. *Solid State Commun.*, **8** (11), 859–865.
46 Loudon, R. (1963) Theory of the first-order Raman effect in crystals. *Proc. R. Soc. Lond. Ser. A Math. Phys. Sci.*, **275** (1361), 218–232.
47 Lee, K.C., Sussman, B.J., Nunn, J., Lorenz, V.O., Reim, K., Jaksch, D., Walmsley, I.A., Spizzirri, P., and Prawer, S. (2010) Comparing phonon dephasing

lifetimes in diamond using Transient Coherent Ultrafast Phonon Spectroscopy. *Diamond Relat. Mater.*, **19** (10), 1289–1295.

48 Liu, M., Bursill, L., Prawer, S., and Beserman, R. (2000) Temperature dependence of the first-order Raman phonon line of diamond. *Phys. Rev. B*, **61** (5), 3391–3395.

49 Ishioka, K., Hase, M., Kitajima, M., and Petek, H. (2006) Coherent optical phonons in diamond. *Appl. Phys. Lett.*, **89**, 231916.

50 Levenson, M., Flytzanis, C., and Bloembergen, N. (1972) Interference of resonant and nonresonant three-wave mixing in diamond. *Phys. Rev. B*, **6** (10), 3962–3965.

51 Klemens, P. (1966) Anharmonic decay of optical phonons. *Phys. Rev.*, **148** (2), 845–848.

52 Menendez, J. and Cardona, M. (1984) Temperature dependence of the first-order Raman scattering by phonons in Si, Ge, and α-Sn: anharmonic effects. *Phys. Rev. B*, **29** (4), 2051–2059.

53 Zverev, P.G., Liu, H., and Basiev, T.T. (1995) Vibrational dynamic of the Raman-active mode in barium nitrate crystal. *Opt. Lett.*, **20** (23), 2378–2380.

54 Herchen, H. and Cappelli, M. (1994) Second-order Raman scattering in diamond up to 1900 K. *Phys. Rev. B*, **49** (5), 3213–3216.

55 Krishnan, R. (1946) Temperature variations of the Raman frequencies in diamond. *Proc. Math. Sci.*, **24** (1), 45–57.

56 Zouboulis, E. and Grimsditch, M. (1991) Raman scattering in diamond up to 1900 K. *Phys. Rev. B*, **43** (15), 12490–12493.

57 Borer, W., Mitra, S., and Namjoshi, K. (1971) Line shape and temperature dependence of the first-order Raman spectrum of diamond. *Solid State Commun.*, **9** (16), 1377–1381.

58 Cui, J.B., Amtmann, K., Ristein, J., and Ley, L. (1998) Noncontact temperature measurements of diamond by Raman scattering spectroscopy. *J. Appl. Phys.*, **83** (12), 7929–7033.

59 Lang, G., Karch, K., Schmitt, M., Pavone, P., Mayer, A.P., Wehner, R.K., and Strauch, D. (1999) Anharmonic line shift and linewidth of the Raman mode in covalent semiconductors. *Phys. Rev. B*, **59** (9), 6182–6188.

60 Cardona, M. and Ruf, T. (2001) Phonon self-energies in semiconductors: anharmonic and isotopic contributions. *Solid State Commun.*, **117** (3), 201–212.

61 Hass, K., Tamor, M., Anthony, T., and Banholzer, W. (1992) Lattice dynamics and Raman spectra of isotopically mixed diamond. *Phys. Rev. B*, **45** (13), 7171–7182.

62 Spitzer, J., Etchegoin, P., Cardona, M., Anthony, T., and Banholzer, W. (1993) Isotopic-disorder induced Raman scattering in diamond. *Solid State Commun.*, **88** (7), 509–514.

63 Vogelgesang, R., Ramdas, A., Rodriguez, S., Grimsditch, M., and Anthony, T. (1996) Brillouin and Raman scattering in natural and isotopically controlled diamond. *Phys. Rev. B*, **54** (6), 3989–3999.

64 Eckhardt, G., Bortfeld, D., and Geller, M. (1963) Stimulated emission of Stokes and anti-Stokes Raman lines from diamond, calcite, and α-sulfur single crystals. *Appl. Phys. Lett.*, **3** (8), 137–138.

65 Penzkofer, A., Laubereau, A., and Kaiser, W. (1978) High intensity Raman interactions. *Prog. Quantum Electron.*, **6**, 55–140.

66 Lang, A.R. (2009) The strain-optical constants of diamond: a brief history of measurements. *Diamond Relat. Mater.*, **18** (1), 1–5.

67 Grimsditch, M., Anastassakis, E., and Cardona, M. (1979) Piezobirefringence in diamond. *Phys. Rev. B*, **19** (6), 3240–3243.

68 Zouboulis, E.S. and Grimsditch, M. (1998) Temperature dependence of the elastic moduli of diamond: a Brillouin-scattering study. *Phys. Rev. B*, **57** (5), 2889–2896.

69 Ramdas, A., Rodriguez, S., and Grimsditch, M. (1993) Effect of isotopic constitution of diamond on its elastic constants: ^{13}C diamond, the hardest known material. *Phys. Rev. Lett.*, **71** (1), 189–192.

70 Loudon, R. (1964) The Raman effect in crystals. *Adv. Phys.*, **13** (7), 423–482.

71 Boyd, R.W. (2003) *Nonlinear Optics*, Academic Press, London.

72 Kovalev, V., Musaev, M., and Faizullov, F. (1984) Stimulated Brillouin scattering gains and decay times of hypersonic waves in optical crystals at the 10.6 μ wavelength. *Sov. J. Quantum Electron.*, **14** (1), 110–112.

73 (a) Sheik-Bahae, M., DeSalvo, R., Said, A., Hagan, D., Soileau, M., and Van Stryland, E. (1992) Nonlinear refraction in UV transmitting materials. *Proc. SPIE*, **1624**, 25–30; (b) Sheik-Bahae, M., DeSalvo, R., Said, A., Hagan, D., Soileau, M., and Van Stryland, E. (1995) Optical nonlinearities in diamond. *Proc. SPIE*, **2428**, 605–609.

74 Zhao, J., Jia, G., Liu, X., Chen, Z., Tang, J., and Wang, S. (2010) Measurement of third-order nonlinear optical susceptibility of synthetic diamonds. *Chin. Opt. Lett.*, **8** (7), 685–688.

75 Kozák, M., Trojánek, F., Dzurnák, B., and Maly, P. (2012) Two-and three-photon absorption in chemical vapor deposition diamond. *J. Opt. Soc. Am. B*, **142** (1), 1141–1145.

76 Arya, K. and Jha, S.S. (1979) Tight-binding bonding orbital model for third-order nonlinear optical susceptibilities in group-IV crystals. *Phys. Rev. B*, **20** (4), 1611–1616.

77 Wherrett, B.S. (1984) Scaling rules for multiphoton interband absorption in semiconductors. *J. Opt. Soc. Am. B*, **1** (1), 62–72.

78 Sheik-Bahae, M., Hutchings, D., Hagan, D.J., and Van Stryland, E.W. (1991) Dispersion of bound electron nonlinear refraction in solids. *IEEE J. Quantum Electron.*, **27** (6), 1296–1309.

79 Van Stryland, E.W., Guha, S., Vanherzeele, H., Woodall, M., Soileau, M., and Wherrett, B. (1986) Verification of the scaling rule for two-photon absorption in semiconductors. *J. Mod. Opt.*, **33** (4), 381–386.

80 Preuss, S. and Stuke, M. (1995) Subpicosecond ultraviolet laser ablation of diamond: nonlinear properties at 248 nm and time-resolved characterization of ablation dynamics. *Appl. Phys. Lett.*, **67** (3), 338–340.

81 Gagarskii, S. and Prikhodko, K. (2008) Measuring the parameters of femtosecond pulses in a wide spectral range on the basis of the multiphoton-absorption effect in a natural diamond crystal. *J. Opt. Technol.*, **75** (3), 139–143.